Comparison of Microwave Versus Conventional Furnace Heat Treatments of Carbide Composite Thermal Spray Coatings

Steven Matthews[1] · Fei Yang[2]

Abstract Thermal spraying has become an industrial standard in the production of wear-resistant WC-Co and Cr_3C_2-NiCr composite coatings. However, generating optimum wear-resistant nano-reinforced carbide microstructures within the coatings remains challenging. The alternative two-step approach in this work involves coating formation under high energy conditions to generate maximum carbide dissolution, followed by heat treatment to precipitate nanocarbides. Microwave heating of particulate materials has been reported to offer several benefits over conventional furnace heating, including faster heating rates, internal rather than external heating, and acceleration of reactions/phase transformations at lower temperatures. This novel work explored the use of microwaves for heat treatment (as distinct from melting) of WC-Co and Cr_3C_2-NiCr thermal spray coatings and contrasted the rate of phase development with that from conventional furnace treatment. Coatings were successfully microwave heat-treated to generate the same phase composition as furnace treatment. Both treatments generated comparable results in the Cr_3C_2-NiCr system. The WC-Co system achieved a much more crystalline structure in a dramatically shorter time relative to the conventional furnace-treated sample. The results are contrasted as a function of material and microstructure interaction with microwaves and the critical phase transition temperatures to account for the observed responses.

Introduction

The two most widely employed hard metal coating compositions are WC-Co and Cr_3C_2-NiCr (Ref 1, 2). WC-based hard metals offer the highest hardness and wear resistance, but their poor corrosion and oxidation characteristics restrict their application to temperatures below 500 °C. Cr_3C_2-NiCr coatings have lower hardness values and wear resistance, but their superior corrosion and oxidation performance sees them employed in corrosive ambient temperature applications and at high temperatures up to 900 °C.

In translating the knowledge from conventional bulk sintered hard metals to hard metal coatings, it is well established that high wear resistance results from the retention of high concentrations of homogeneously distributed, very fine (preferably submicron) carbide grains within a continuous tough, ductile metallic binder (Ref 3-6). However, the majority of hard metal feedstock powders for thermal spraying employ carbide particles of approximately 1-5 μm (Ref 7-12). This is driven by the unique conditions under which thermal spray coatings are formed. In flight, melting of the metallic binder leads to dissolution of the solid carbide grains and potentially their peritectic decomposition under extreme heating. The dissolved carbon is prone to reacting with surrounding oxygen to form CO/CO_2, reducing the coating carbon content and the

✉ Steven Matthews
s.matthews@auckland.ac.nz

1 Department of Chemical and Materials Engineering, The University of Auckland, Auckland, New Zealand

2 Waikato Centre for Advanced Materials and Manufacturing, School of Engineering, University of Waikato, Hamilton 3240, New Zealand

concentration of the desired carbide phases, as well as leading to the formation of undesirable sub-carbides (e.g., W_2C, Cr_7C_3 and $Cr_{23}C_6$) (Ref [1], [2], [13-21]). Furthermore, the dissolved carbide elements become trapped within the metallic binder during rapid solidification, generating brittle supersaturated phases prone to brittle fracture during wear (Ref [20], [21]). As the carbide grain size is reduced, these negative effects are exacerbated due to the dramatic increase in carbide surface area, typically leading to poor wear responses (Ref [7], [8], [22], [23]).

In an alternative approach to generating nanocarbide-reinforced coatings, a two-step mechanism has been postulated and explored for these compositions (Ref [14], [15], [17], [24]). The first step takes advantage of the tendency for carbide grains to dissolve into the molten binder in flight, by using high thermal input plasma thermal spraying to maximize the extent of carbide dissolution and peritectic decomposition. Carbon loss is minimized through the use of a protective argon gas shroud. Rapid solidification of the highly dissolved particles at impact generates a supersaturated and very brittle coating. Post-coating heat treatment is then employed to precipitate the dissolved carbide elements and return the coating composition to that of the feedstock (subject to the effects of carbon loss). However, by controlling the kinetics of precipitation and grain growth through the time and temperature of heat treatment, it should be possible to tailor the microstructure from nanocarbide-reinforced composites through to complex interconnected carbide networks (Ref [16], [17], [24]).

While smaller lab-scale samples can be really heat-treated in conventional resistance element furnaces, this heat treatment approach poses a number of challenges when attempting to scale up to industrial application. In particular, furnace heating is slow and therefore expensive both in heating and cooling, involves heating the entire substrate beneath the coating and thus potentially altering its grain size and microstructure, and potentially leads to variations in thermally induced changes with coating depth due to the outside-to-inside heat flux. Point source heating methods, such as combustion flames or lasers, are significantly quicker in heating the surface of the sample. However, they rely on energy being applied to the surface and then transferred into the body of the sample via thermal conduction. The resulting temperature gradient leads to a corresponding gradient in the phase/microstructure transformations with depth. Microwave heating offers an alternative approach that is reported to overcome many of these challenges (Ref [25-30]). Heating is induced within the material by interactions of the microwave with the atoms, generating a hotter interior than exterior (Ref [31]). This leads to more uniform volumetric heating and homogeneous thermally induced phase/microstructure

transformations. Faster processing times restrict grain growth and phase/microstructure degradation, leading to superior mechanical properties (Ref [26], [31-34]). Furthermore, several reports have indicated the potential "catalytic effect" of microwave irradiation in regard to speeding up chemical reactions (Ref [28], [35]). Microwave processing has been applied extensively to bulk carbide composites for liquid-phase sintering (Ref [33]).

Microwave Interactions with Metals

Fundamentally, the low penetration depth of microwaves in metals should preclude the microwave processing of metallic materials (Ref [26], [27]). While this is true for bulk metals, it has been shown that, in powder form, mixtures containing metal powders can be heated (Ref [26-28]), while 100% metal powders can also be sintered to full density (Ref [26-28], [36]). The mechanisms accounting for the temperature rise in metal powders remain an area of debate, with several theories postulated. One theory posits that, while the "skin depth" of microwave penetration is only several microns, metal powders form a large surface area or "skin" area that can interact with the microwaves, generating uniform heating (Ref [27]). While this readily accounts for the results of nano- or submicron powders, the theoretical limit of particle size for this effect is less than 100 μm (Ref [27]). For particles greater than 100 μm, the outer skin is directly heated to the "skin depth," with this hot layer then heating the internal material through direct thermal conduction.

In an alternative hypothesis, Rybakov (Ref [37], [38]) postulated that metal powder heating was achieved due to the effect of thin, nonconducting oxide layers that form on the surface of each particle. Such oxides dramatically reduce the effective conductivity of the powder particles when contacted together and significantly increase the electromagnetic power that can be absorbed (Ref [26]).

However, Cheng, Roy and Agrawal (Ref [36]) argue that skin depth absorption alone could not account for their results, showing full sintering of large complex-shaped compacts (100 mm diameter with a mass of 1 kg) in 30 minutes within a 2.45 GHz multimode microwave system. They postulate that this was due to past theories primarily attributing energy absorption to dielectric loss factors. By exploiting the variation in the intensity of the electric field distribution and magnetic field distribution within their microwave heating system, they were able to contrast the heating of samples in zones dominated by the electric field or magnetic field effects. By plotting sample temperature as a function of time in each field, they conclusively showed the different materials exhibited very different heating behaviors in electric field and magnetic field dominated microwaves. Conductive powder samples, such

as powdered metals, were much more efficiently heated in the magnetic field, while insulators were more effectively heated in electric field. In contrasting metallic powder with the bulk metal the same composition, the powder samples were effectively heated, while no change occurred in the bulk sample. They highlighted that the formation of eddy currents was a significant contributing factor to the heating mechanism under the magnetic field, which has since been supported by other works (Ref 26).

An important contributing factor to metal powder heating by microwaves is that the ability of metals to couple with microwaves increases with increasing temperature above the critical temperature (typically 400-500 °C)(Ref 27). A contributing factor to this is that the resistivity of metals increases with increasing temperature, thereby increasing the microwave penetration depth (Ref 26).

The effect of microwaves on the fundamental mass transport mechanisms occurring at high temperatures is still a point of conjecture. Vetli (Ref 39) postulated that the high-frequency electric field acting between metal particles generates a plasma, which promotes mass transport in the contact zones between the particles. As such, particles that are closer together, but not touching, can still be sintered together, e.g., crack healing. In contrast, Saitou (Ref 29) noted no change in the sintering mechanism for respective metallic powders when sintered by microwave and electric furnace, based on the consistent activation energies for sintering seen in both. However, they did note changes in the pre-exponential constants of the Arrhenius functions modeling the shrinkage response. These factors are closely linked to the effect of several material parameters, e.g., vacancy concentration, surface energy, atomic vibration frequency, etc., suggesting that microwaves have some effect at this fundamental level (Ref 29). Intriguingly, this work also observed a reduction in the crystallographic phase transformation temperatures of iron particles in microwave heating (875 °C versus 910 °C for the BCC to FCC transition, and a 100 °C reduction in the FCC to BCC transition at 1390 °C). They postulated that microwave radiation lowered the free energy of the high-temperature phase, lowering the transition temperature. However, the mechanism accounting for this remains unknown.

Microwave Interactions with Composite Materials

The response of composite materials to microwave radiation is highly dependent upon the absorption of the electromagnetic energy by the matrix and reinforcement phases. Where only one material interacts with the microwave and heats up, it will heat the remaining material through conventional thermal conduction mechanisms (Ref 26, 27, 40). However, quantifying the depth of microwave penetration, and hence the depth of heating, is complex and dependent also on the size, morphology and distribution of the phases (Ref 41).

Because of the unique characteristics of rapid and volumetric heating induced by microwave processing and the potential to retain ultrafine WC grains (Ref 41), it has been widely investigated in the area of WC-Co hard metals/composites (Ref 26, 30, 32, 33, 36, 40-46). In general, it has been found that for bulk sintered WC-Co composites, microwave-induced sintering could be achieved at much shorter processing times, primarily due to the rapid heating rates achievable and the uniformity of heating throughout the part. The shorter processing time leads to significantly less WC grain growth (without the use of grain growth inhibitors), enabling the retention of smaller, more wear-resistant carbide structures, and less W dissolution into the Co binder (Ref 26, 41, 44). The finer microstructures were reflected in the superior hardness and wear resistances reported versus materials processed using electric furnace heating (Ref 34, 44, 47).

Microwave treatment has also been used to generate clad layers onto bulk metallic substrates of different compositions (Ref 46-49). In this approach, carbide containing powders were manually applied as a layer on the substrate, covered with a suitable solid or powder susceptor material, and then processed under microwaves to melt the powder onto the surface. WC-Co (Ref 46), Ni-20-30wt.% Cr_3C_2 (Ref 47, 48) and Ni-10wt.% (WC-8wt.%Co)-10wt.% Cr_3C_2 (Ref 49) have all been successfully processed in this way.

To date, few works have applied microwave processing to thermally sprayed coatings (Ref 45, 50). Prasad et al. treated high velocity oxygen fuel (HVOF)-sprayed CoMoCrSi-30wt.% Cr_3C_2 coatings to fuse them to a titanium substrate (Ref 50). Medabalimi et al (Ref 45) microwave-treated HVOF-sprayed WC-CrC-Ni (66.95W-19Cr-7.25Ni-6.8C (wt.%)) and NiCrFeSiB-35wt.% WC-Co (47.6Ni-29.2W-9.4Cr-4.2Co-2.8Si-2.8Fe-2C-1.9B (wt.%)) powders onto Fe-based boiler tube substrates. The coatings were covered in graphite and SiC susceptors to generate a hybrid "thermal + microwave" heating approach. In both cases, the aim was to "remelt" the coating to fuse into the substrate. The aim of the current work was distinctly different. Our intention was to only heat-treat the coatings to reprecipitate dissolved phases, not to re-melt the metallic binder phase. To the best of our knowledge, this is the first work to consider microwave processing for such treatment. Furthermore, the current coating compositions of Cr_3C_2-25wt.%NiCr and WC-17wt.%Co are significantly richer in the carbide phases compared to the previous thermal spray coating compositions processed by microwaves and more akin to the bulk hard metals discussed previously. The difference here, however, is that the composition and microstructure of the sprayed composite coatings undergo

dramatic changes due to carbide dissolution/decomposition, rapid solidification upon impact to form metastable supersaturated compounds and subsequent precipitation of phases from this state (Ref 14, 15, 17, 24, 51, 52). As such, the electromagnetic material properties vary dramatically with time, generating a novel extension to the previous studies in the literature on WC-Co, but also to the very limited work on Cr_3C_2-NiCr composites. One of the greatest advantages of microwave processing is the rapid increase in temperature to the target set point and the faster system cooling rate, which dramatically reduces the exposure time of the material compared to the slow heating and cooling cycles in conventional electric furnace treatment. However, this makes it challenging to comment on the fundamental effect of microwave treatment over and above its rapid temperature changes. To overcome this, the current work exploited the rapid heating rate in microwave treatment, while also inserting samples into preheated electric furnaces. Samples were heat-treated for periods of 5, 10, 30 and 60 minutes at 900 °C. Previous thermal analysis of these coatings had highlighted that this was the minimum treatment temperature required to ensure a full transformation of the metastable phases formed in the as-sprayed coatings (Ref 24, 52). The treatment durations were selected to enable sufficient grain growth to occur in order to analyze the precipitates formed. By exploring a range of treatment times, it was hoped to explore the variation in the kinetics of thermally induced transformation between the two techniques. The microwave-treated samples were allowed to furnace cool, while the electric furnace samples were removed and allowed to air cool on ceramic blocks on top of the furnace. As such, this work enables a direct comparison of microwave and thermal heat treatment for the same durations of treatment. In addition to the potential difference in phase change kinetics, there was particular interest to also investigate the effect of crack healing. It has been postulated that microwave treatment of neighboring but non-contacting particles can still lead to particle sintering and so-called "crack healing." Thermal spray coatings are formed from the mechanical bonding of interlocking "splats," a characteristic which generates a very high internal splat–splat interface surface area, or effectively an internal crack network. Preferential "healing" of this splat interface/crack network would be a major advantage to the application of thermal spray coatings. Microhardness testing was employed to assess any potential changes in the strength of the coating splat microstructure with the treatment. The compositional and microstructural changes as a function of treatment technique and time were assessed via XRD and cross-sectional electron microscopy using backscatter electron imaging.

Experimental Procedure

Agglomerated and sintered powders of nominal composition WC-17wt.%Co (Diamalloy 2005NS, nominal size − 45/ + 5.5 μm)(Oerlikon Metco, USA) and 75wt.% Cr_3C_2-25wt.%NiCr (Amperit 588.074, nominal size − 45/ + 15 μm) (Hoganas AB, Sweden) were sprayed onto degreased and gritblasted 15 mm × 15 mm × 3 mm Alloy 625 substrates using a shrouded SG-100 plasma spray system (Praxair Surface Technologies, USA) under the conditions of Table 1. The deposition conditions were selected to minimize the extent of carbon loss and excessive carbide dissolution/decomposition in order to simplify the compositional developments with heat treatment (Ref 14, 17, 24, 51, 52). A layer of Ni20Cr (Ni106, nominal size − 63/ + 11 μm) (Praxair Surface Technologies, USA) was sprayed on top of the WC-Co coatings to provide protection against oxidation during the treatment. The Cr_3C_2-NiCr was not coated due to its high temperature corrosion resistance.

The coated samples were heated to 900 °C and held for periods of 5, 10, 30 and 60 minutes using microwave heating and conventional electric furnace heating. Microwave heat treatment was performed in the same adapted microwave furnace (Panasonic Thermowave Mod.III multimode microwave system equipped with a water cooling system) as described in (Ref 53) at 1.3 kW and 2.45 GHz. The coating samples, together with SiC susceptors, were placed within a thermal insulation chamber within the microwave. A type-B thermocouple, sheathed in platinum foil, passed through the lid of the thermal insulating chamber to sit just above the samples and was used to control the temperature. Heat treatment was performed in air. Samples were heated at ≈100 °C/min to 900 °C and held for the test duration, before the microwave was turned

Table 1 Spray parameters

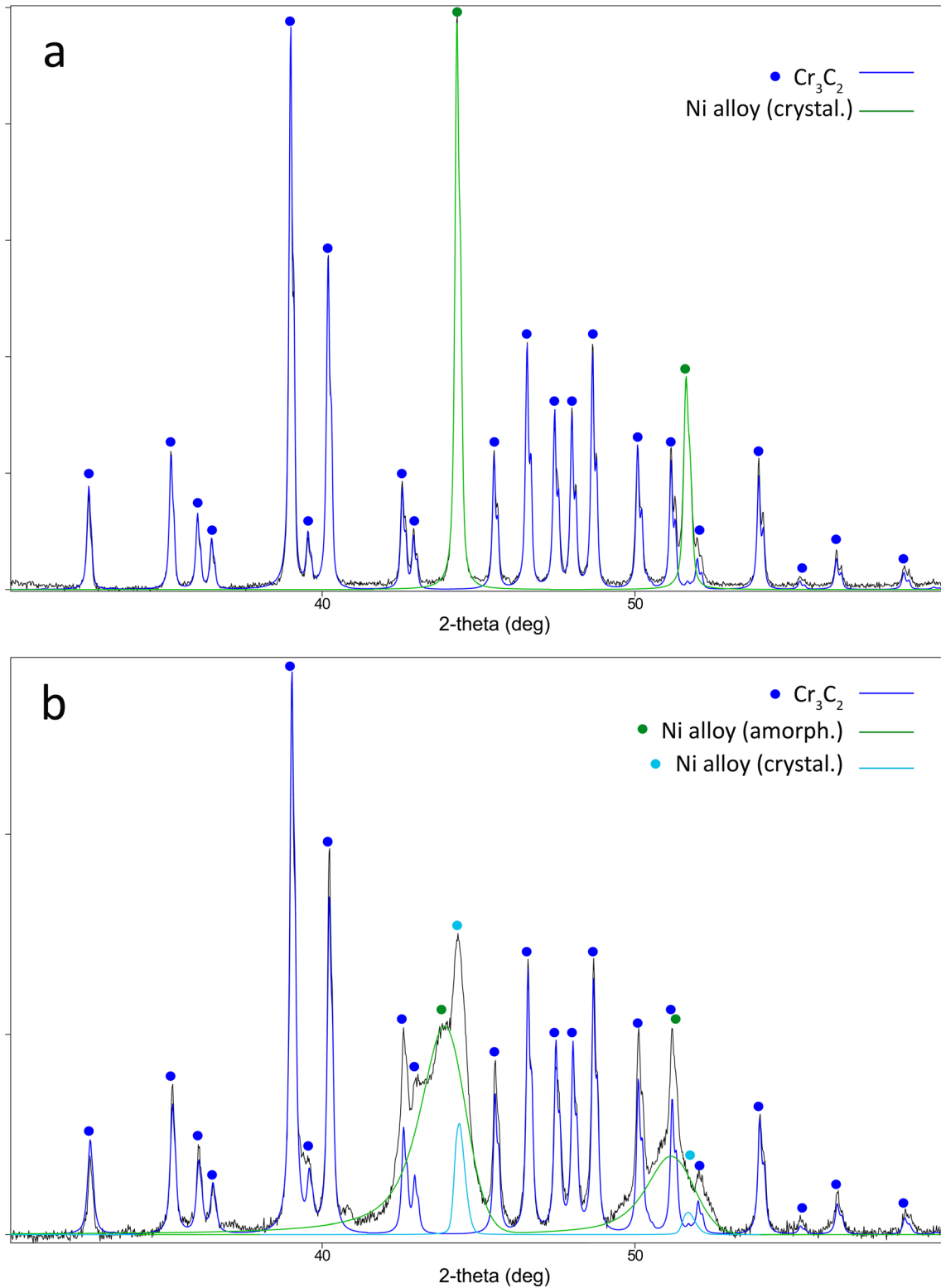| Spray torch	SG-100 (Praxair Surface Technologies, USA)
Nozzle	Mach II (P/N 2083-100)
Primary gas	Argon, 40 SLPM
Secondary gas	Helium, 18 SLPM
Current	900 A
Voltage	75 V
Powder feed rate	40 g/min (WC-Co), 30 g/min (Cr_3C_2-NiCr)
carrier gas	Argon, 4 SLPM
Spray distance	100 mm
Traverse speed	500 mm/s
Shroud gas	Argon, 300 SLPM

Fig. 1 XRD patterns for the Amperit 588.074 Cr₃C₂-25NiCr powder (a) and the as-sprayed coating (b), with the phase peaks fitted from Rietveld analysis
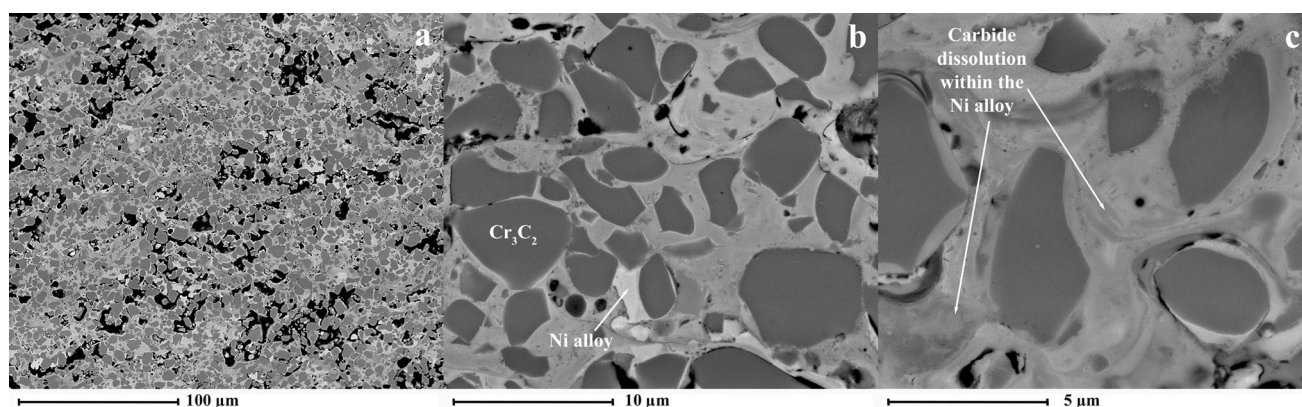
Fig. 2 Cross sectional BSE images of the Cr_3C_2-25NiCr as-sprayed coating

off and the samples allowed to furnace cool. On average, the samples cooled to 800 °C within 3.5 minutes, 600 °C in 13 minutes and 400 °C in 29 minutes. The samples were removed once the temperature dropped to 120 °C.

The electric furnace heat treatment samples were first wrapped in 309 stainless steel foil to further protect from oxidation (Note: this could not be done in the microwave trial due to sparking tissues). Samples were inserted into a box furnace preheated to 900 °C and removed and allowed to cool on a ceramic installation block in air after treatment. The cooling rate was not monitored as the samples were wrapped in foil. The furnace took an average of 5 minutes to return to the 900 °C set point after adding a sample, after which the test time was started. The variation in heating and cooling rates between the microwave and furnace trials was an unavoidable source of error. However, given the exponential variation in diffusion with temperature, it is assumed that changes occurring within the samples treated by both systems were comparable for the same treatment times at 900 °C, particularly those with longer dwell times of 30 and 60 minutes.

The top coating surface was ground and polished to a 3 μm finish on all samples prior to analysis. In the WC-Co samples, this was to ensure removal of the protective Ni20Cr layer and any potential interdiffusion layer. In the Cr_3C_2-NiCr coating, this was to ensure the removal of the surface oxide layer as well the near surface material that was affected by diffusion of oxide forming elements to the surface. X-ray diffraction (XRD)(Ultima IV combined with D/TEX Ultra linear detector using Cu Kα x-rays)(Rigaku, Japan) characterized the phase composition of the starting powders and coatings. XRD patterns were collected from $2\theta = 20\text{-}80°$ at 0.02°/step. Rietveld analysis was performed using the Rigaku PDXL2 analysis software. The background was manually fitted in each pattern to avoid challenges of the software attempting to improve the "goodness of fit" by refining the broad peaks from amorphous/nanocrystalline material. Peaks were fitted with a "split pseudo-Voigt"

model, in which the lattice parameter peak profile parameters were refined to achieve the best fit. The crystal structure of each phase was assumed to match that of the database pattern and was not refined. While the as-sprayed coating structures were rapidly solidified, preferential orientation was also not considered as part of the peak fitting analysis. It should be noted that the coating samples consisted of a complicated mixture of crystalline, nanocrystalline and metastable, supersaturated phases, making quantitative analysis a challenge. The degree of fitting and quantification was, therefore, not expected to reach "perfect" refined values. Therefore, this analysis gives a first approximation of the variation in concentrations of the main coating phases as a function of deposition technique.

Cross-sectional samples were mounted on epoxy under vacuum, prior to grinding and polishing to a 0.05 μm finish. Scanning electron microscopy (Quanta 200)(FEI, USA) analyzed the coating cross sections using backscatter electron imaging (BSE). Image analysis was performed using ImageJ.

The Vickers microhardness (Struers Durascan, Denmark) was measured on the coating cross sections for a duration of 10 seconds. A minimum of 20 indents were taken per sample to establish a representative average and standard deviation. The high velocity, low thermal input conditions used to spray the coatings led to a high level of internal porosity within the Cr_3C_2-NiCr coating. In order to prevent the porosity from dominating the hardness readings, test loads of 100 g, 200 g and 300 g were trialed. The 300 g load led to excessive cracking and linkages between the pockets of porosity. The 100 g load generated indents only slightly larger than the carbides in the coating, leading to very heterogeneous results as a function of the localized microstructure. The 200 g load was, therefore, used to generate indents large enough to reflect the average microstructural response, without leading to excessive cracking into porosity features. This load was used on both coating compositions.
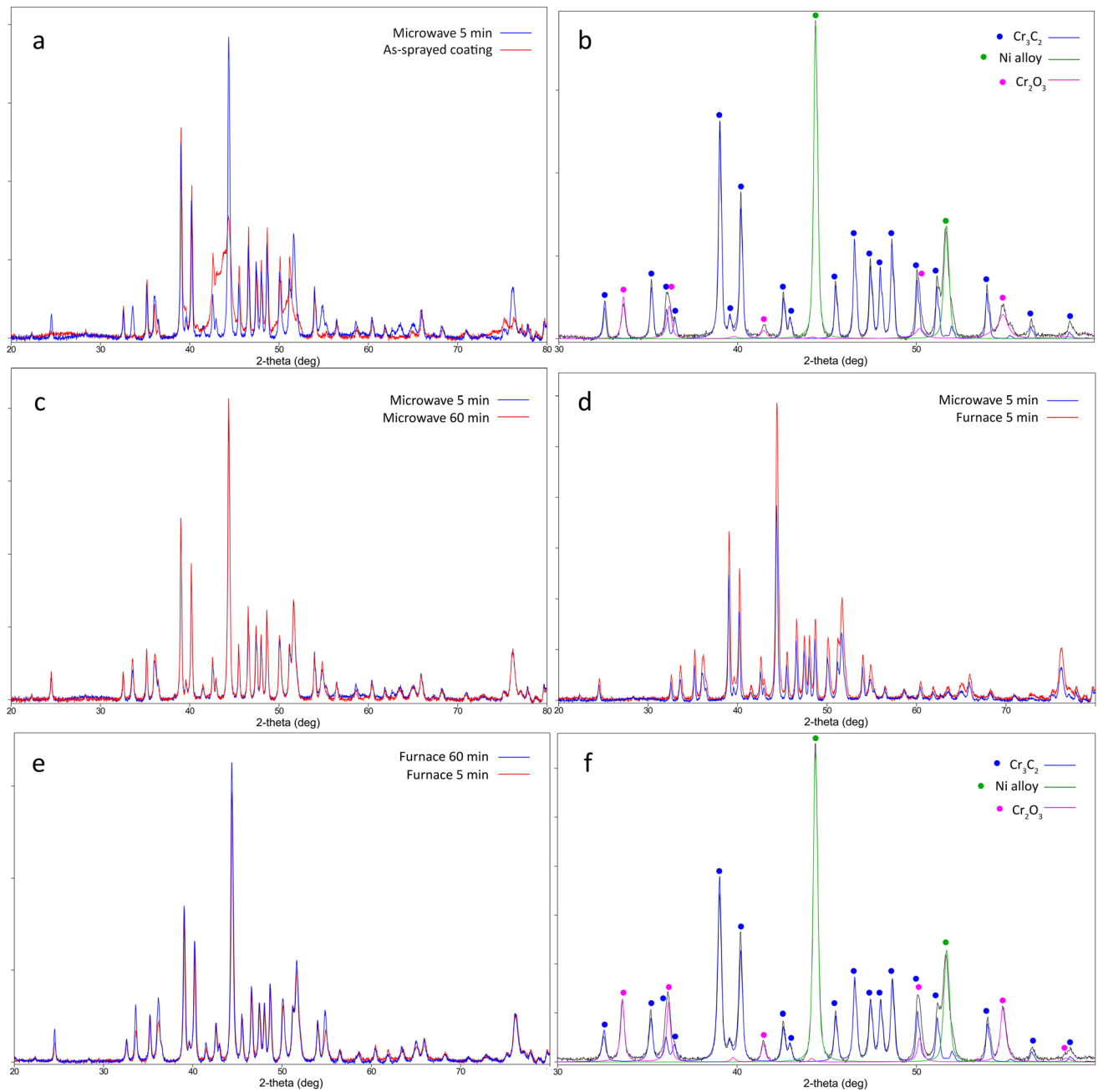
Fig. 3 XRD patterns for microwave and furnace heat treated Cr$_3$C$_2$-NiCr coatings – Overlay of the 5-minute microwave heat-treated sample over the as-sprayed coating (a), the Rietveld fitted pattern of the 5-minute microwave heat treated coating (b), the overlay of the 60 minute and 5-minute microwave heat-treated coatings (c), the overlay of the 5-minute microwave and furnace heat-treated samples (d), the overlay of the 60 minute and 5-minute furnace heat-treated coatings (e), and the Rietveld fitted pattern of the 60 minute furnace heat-treated coating (f)

Results

Cr$_3$C$_2$-NiCr Coatings—Powder and As-sprayed Coating Characterization

The agglomerated and sintered powder exhibited the characteristic spherical morphology of this manufacturing technique, with notable internal porosity between the grains of the discrete dark contrast Cr$_3$C$_2$ carbides and bright contrast metallic NiCr binder phases (Ref 17). XRD indicated the presence of only Cr$_3$C$_2$ (JCPDS 01-071-2287/ICSD 015086)(76.8wt.%) and a Ni alloy (JCPDS 01-089-7128/ICSD 076667)(23.2wt.%), with the Ni peaks shifted to lower 2θ positions on account of the alloying with Cr, Fig. 1(a).

The low thermal input spraying conditions were reflected in the formation of dense zones in the coating, punctuated by localized pockets of globular porosity, Fig. 2(a). High concentrations of globular carbides were retained (48.2vol.% based on image analysis, 42 wt.% based on Rietveld analysis), surrounded by zones of mid-gray metallic bond of varying grayscale contrast (51.8 vol.% based on image analysis, 58 wt.% based on Rietveld analysis). The darker contrast of the Ni binder within the dense zones compared to the very bright contrast Ni in the poorly molten zones was indicative of carbide dissolution into the molten binder phase in flight. The retention of the larger-sized carbides indicated that it was the smallest carbides which preferentially underwent dissolution, while the larger carbides only underwent peripheral dissolution, as evident by their rounded morphologies. Higher magnification images highlighted the "swirls" of grayscale contrast within the metallic binder and isolated examples of submicron size precipitates, Fig. 2(b) and (c). These highly localized degrees of carbide dissolution into the metallic binder indicate that limited mixing occurred within the binder in flight, generating a highly heterogeneous binder composition between the retained carbide grains. The XRD pattern reflected the limited thermal input during spraying, with peaks of Cr_3C_2, a crystalline Ni alloy and a more highly alloyed amorphous/nanocrystalline Ni alloy phase (Ref 17), Fig. 1(b). No oxides or sub-carbide phases were found. Rietveld quantification generated a composition of 40.3 wt.% Cr_3C_2, 19.8 wt.% crystalline Ni alloy and 39.9 wt.% amorphous/nanocrystalline Ni alloy, which was comparable with the image analysis results.

## Cr_3C_2-NiCr Coatings—Heat Treatment Analysis

XRD Analysis

Within the first 5 minutes of microwave heat treatment, the as-sprayed coating composition totally transformed back into the equilibrium phases of Cr_3C_2 and a Ni alloy, Fig. 3(a) and (b). The microwave 5-minute pattern was a close match to that of the starting powder, with the only differences being the formation of Cr_2O_3 (JCPDS 01/082-1484/ICSD 075577) in the coating and the shift in the Ni alloy peak to a higher 2θ (lower d-spacing) position. The Ni peak shift was postulated to result from the reduction in Cr alloying due to oxide formation. No changes occurred in the coating phases with increasing treatment to 60 minutes, Fig. 3(c). The only subtle change was the slight increase in relative intensity of the oxide phase. Note that the surface of the coatings was ground and polished prior to XRD analysis, meaning that the oxide detected had formed within the coating (not at the surface) and justifying the only minor increases in concentration.

Fig. 4 Rietveld quantified composition of the Cr_3C_2-NiCr coatings as a function of microwave and furnace heat treatment time, including the Cr_2O_3 oxide (a), and without the oxide (b), together with the "a" lattice parameters for the Cr_3C_2 carbide (c) and Ni alloy (d) phases. The separation distance between the main Cr_3C_2 and Ni XRD peaks for both treatments is plotted in (e), together with the crystallite sizes of the Cr_3C_2 (f) and Ni alloy (g) based on the Scherrer equation ▶

The 5-minute furnace heat-treated sample XRD pattern was an extremely close match to that of the microwave-treated sample, Fig. 3(d). While a subtle shift in peak positions occurred, these were observed uniformly over the whole pattern, implying a physical sample alignment error, instead of a difference in the phases themselves. Again, no significant changes in the XRD patterns were observed out to 60 minutes of treatment, Fig. 3(e) and (f). This was confirmed by cross correlating the 60-minute XRD patterns from both treatments, which were close matches to each other.

The quantified compositional changes with time, based on Rietveld analysis, were a close match for both the microwave and furnace-treated samples, Fig. 4(a). Any subtle variations were assumed to be within the experimental error, given the variability in the fitting of the XRD patterns. In contrasting the coating compositions with the starting powder, it can be seen that the Ni binder contents return to values close to the starting composition, while the Cr_3C_2 content is notably lower. The reduction in Cr_3C_2 content from the powder correlates to the same order of magnitude as the Cr_2O_3 formation. However, it is not a direct correlation to presume that the reduction in Cr_3C_2 occurred due to preferential oxidation to form the Cr_2O_3. While some oxide formation on Cr_3C_2 undoubtedly occurred, the majority is thought to form on the metallic binder phase material based on previously reported oxidation studies (Ref 54). Instead, the reduction in Cr_3C_2 content is attributed to carbide rebounding during coating formation (Ref 55), especially given the limited degree of carbide dissolution and high impact velocity. If the oxide content is removed and the data normalized, the coating compositions become a lot closer to those of the starting powder, Fig. 4(b). The furnace-treated results remained remarkably consistent, while the microwave data appeared to show a gradual reduction in Cr_3C_2 content and concurrent increase in the Ni binder content. Further work is required to establish if the subtle trend reflected a slow compositional development, or if the variability was within the data fitting experimental error. The steady-state coating compositions of only Cr_3C_2 and NiCr alloy at the recorded concentrations exist within a very small window of the ternary Cr-Ni-C phase diagram at this temperature (Ref 17, 56). This implies that very little carbon was lost during
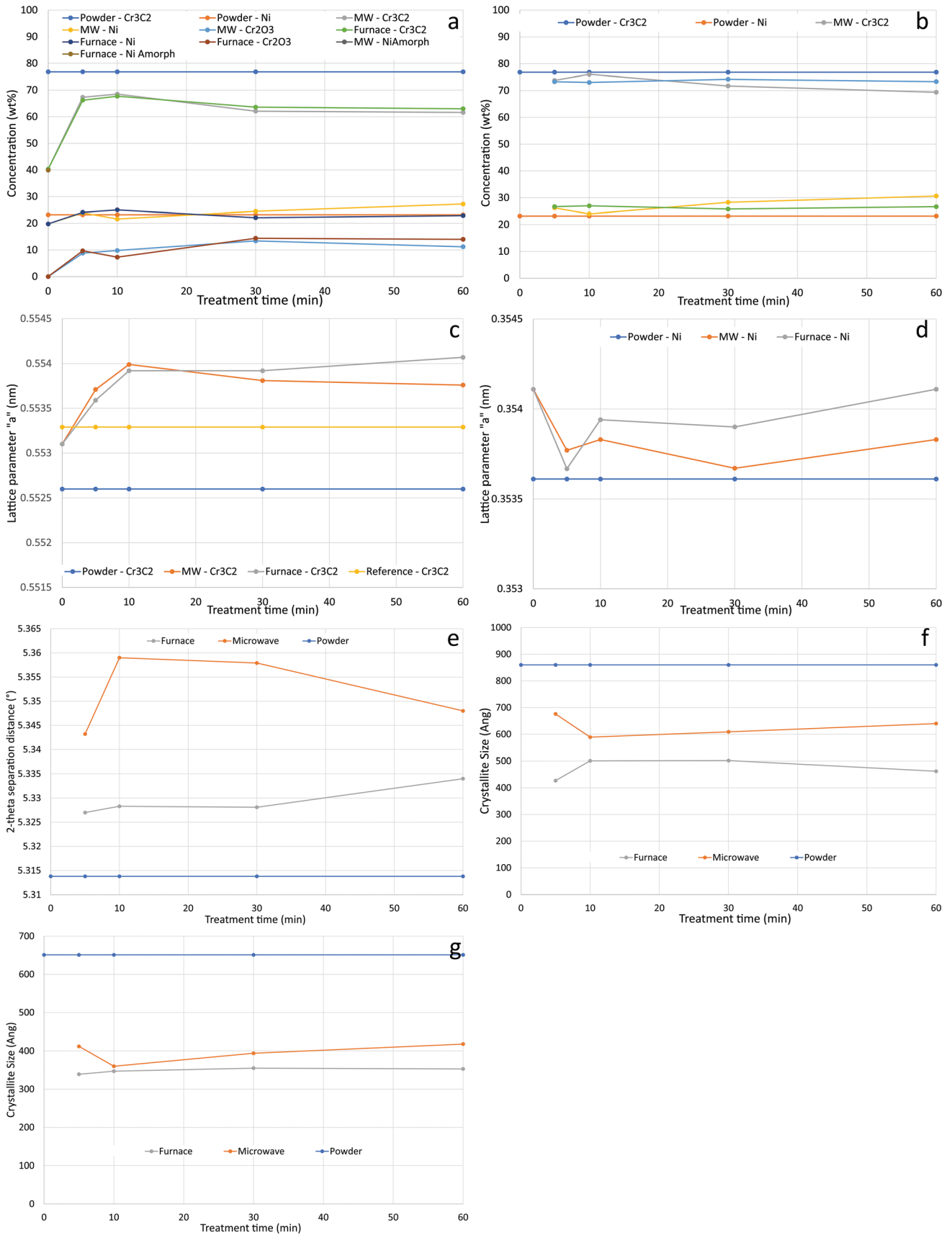
spraying, otherwise the sub-carbide Cr_7C_3 (JCPDS 01-089-5902/ICSD 087129) would have been expected to form.

Figure 4(c) plots the "a" value of the Cr_3C_2 lattice parameter. The powder data were notably smaller than the 0.55329 nm reference value in the Ni-Cr-C system (Ref 56). This is postulated to be a result of the physical height setting of the highly spherical powder in the sample holder during analysis rather than a phase-based compositional effect, as there is no obvious mechanism to account for such a lattice shift. The as-sprayed coating was a close match to the Cr_3C_2 reference. Interestingly, a broader distribution of lattice values for Cr_3C_2 have been presented in a review of the Cr-C binary system, Table 2 (Ref 57). The variation in lattice parameter was attributed to small homogeneity ranges. The as-sprayed coating should, in principle, match that of the starting powder since it reflects the retained Cr_3C_2 grains that did not undergo dissolution into the molten Ni binder and hence, should have remained unchanged. Following the treatment by both methods, the lattice parameter increased out to 10 minutes, beyond which it remained stable. Increases in the Cr_3C_2 lattice parameter can be seen from analysis of the ternary Cr-Ni-C system, typically from direct solidification from the liquid phase, Table 2. The steady-state values of this work fall within the mid to upper end of this range, supporting the hypothesis that the precipitated Cr_3C_2 phase was alloyed, and potentially saturated, with Ni. However, the maximum solubility of Ni in Cr_3C_2 is only 0.7 at.%, and so this is expected to have only a minor influence on Cr_3C_2

properties. This high value is justifiable given that such rapid precipitation within 5 minutes could only occur by the incorporation of elements within the immediate area precipitation, i.e., within the diffusion length of Cr and Ni at this time and temperature. The driving force for precipitation from the supersaturated Ni binder in the as-sprayed state appears to exceed the metastability of the Ni saturated Cr_3C_2 crystal structure at this temperature.

Figure 4(d) summarizes the Ni lattice parameter values of the powder and coatings. The powder value of 0.35361 nm correlates with a Cr content of ≈ 12.8 at.% (Ref 58). As for the Cr_3C_2, this is believed to be shifted to lower values due to changes in sample height caused by the free-flowing nature and settling of the spherical particles during XRD preparation and analysis. The crystalline as-sprayed coating Ni lattice value of 0.35441 nm corresponded to a Cr content of 17.5 at.%. As this highly crystalline Ni alloy is believed to be unmolten or poorly molten material carried on from the starting powder, it is believed to be a more accurate reflection of the feedstock powder Cr content. The amorphous Ni alloy lattice parameter of 0.3574 nm corresponded to a Cr content of ≈ 37-38 at.%. This is close to the solubility limit at 900 °C (Ref 58) and highlights a significant degree of Cr alloying from carbide dissolution. As such, it is also assumed to contain a significant magnitude of C alloying, meaning that the Cr concentration could vary from that predicted from the Ni-Cr equilibrium alone. With heat treatment, the Ni lattice parameter decreased as Cr and C precipitated out of the metallic binder to form Cr_3C_2. Aside from the 5-minute furnace sample, the Ni lattice values remain comparable for both heat treatment techniques, and stable with increasing time at values of 14.5-18 at.% Cr based on the Ni-Cr equilibrium (Ref 58).

In order to confirm this conclusion, Fig. 4(e) plots the 2-theta separation distance between the main Cr_3C_2 peak at 39° and the primary Ni peak at 44.4°. This analysis had the added benefit of removing the effect of subtle sample to sample variations, overcoming the influence of bulk pattern shifts due to physical height setting challenges. If it is assumed that the Cr_3C_2 lattice parameter does not change significantly, then it effectively acts as an internal reference position. Any change in the separation between these two peaks is then indicative of the Ni alloy peak shift. An increase in separation means a Ni alloy shift to higher 2-theta, implying a lower d-spacing, and, therefore, a reduction in Cr alloying. Note that the as-sprayed coating data have not been plotted due to the complex mix of crystalline and nanocrystalline material. Both treatments generate an immediate increase in separation distance over the first 10 minutes, constant values out to 30 minutes but then contrasting responses from 30 to 60 minutes. These data indicate more definitively than the lattice parameters

Table 2 Summary of Cr_3C_2 lattice parameters values

Reference state of formation reaction	Lattice parameter/nm
Pure Cr_3C_2 reference	0.55329 ± 0.00005 (Ref 56)
	0.551 (Ref 57)
	0.552 (Ref 57)
	0.5531 (Ref 57)
	0.5537 (Ref 57)
	0.5545 (Ref 57)
	0.5535-0.5545 (neutron diffraction) (Ref 57)
Cr_3C_2 with Ni substitution in solid solution (assumed to be measured at ambient temperature from samples quenched from reaction temperature)	
$L \leftrightarrow (Ni) + Cr_3C_2 + C$	0.5537 ± 0.00005 (Ref 56)
$L + Cr_7C_3 \leftrightarrow (Ni) + Cr_3C_2$	0.5544 ± 0.00005 (Ref 56)
As cast samples with $Ni + Cr_3C_2$ compositions	
Cr 24 at.%, C 10 at.%	0.548 ± 0.01 (Ref 56)
Cr 23 at.%, C 10 at.%	0.552 ± 0.005 (Ref 56)
Cr 18 at.%, C 10 at.%	0.5536 ± 0.003 (Ref 56)
Cr 29 at.%, C 25 at.%	0.5526 ± 0.002 (Ref 56)

data in Figure d, that microwave treatment led to a faster rate of Ni alloy compositional change, and to a much lower Cr content relative to the furnace-treated coating. Higher-resolution analysis, such as TEM-based EDS or selected area diffraction, is required to more accurately quantify the Ni alloy Cr content, but was beyond the scope of this work.

Figure 5(f) and (g) plots the crystallite size of the Cr_3C_2 and Ni alloy, based on the peak width of their most intense peaks using the Scherrer equation function in the XRD software. Only one peak was used due to complications of peak overlap when attempting to quantify this from the full phase pattern. The carbide crystallite size in the coatings is a volume average value incorporating both the large retained carbide grains and the smaller precipitate grains. The coating crystallite sizes were smaller than that in the powder, indicative of the high concentration of precipitated grains. However, it is notable that the microwave-treated coating had a distinctly larger average crystallite size compared to the furnace-treated sample, implying that faster precipitate crystallite growth had occurred. In addition, the data suggest that little crystallite growth occurred after 10 minutes of treatment. The Ni alloy crystallites reached steady state within the first 5 minutes of both treatments and showed only subtle changes beyond that.

SEM Analysis

After 5 minutes of microwave heat treatment, low-magnification images indicated no change in the bulk porosity of the coating, which was now lined with internal oxide formation, Figure 5(a). In the dense zones, widespread carbide precipitation had occurred homogeneously throughout the entire coating, Fig. 5. Any localized variation in precipitation density was postulated to result from the variation in the initial extent of localized carbide dissolution, rather than the procedure of heat treatment, Fig. 5(b). High magnification images highlighted a continuous spectrum, from isolated individual precipitates between large retained carbides in low dissolution zones, through to bands of closely precipitated grains agglomerating to form larger lattice structures. However, the microstructure was dominated by homogeneous carbide precipitates that formed uniformly throughout the inter-carbide zones within the Ni alloy, Fig. 5(c), (d), (e) and (f). While precipitation occurred on the surface of retained carbides, this did not occur preferentially to that within the matrix dominated zones. The grain orientation also appeared to be randomly distributed, without an obvious axis of preferred orientation. The precipitated carbides all appeared to be of the same grayscale contrast, implying a uniform precipitate composition. The microstructure and morphology the precipitates mirror those presented in the literature (Ref 52),

and so the same mechanism of development was assumed to have occurred here.

Continued microwave heat treatment up to 60 minutes led to only subtle changes in the microstructure, Fig. 6. In some zones, it appeared that the carbide grains increased in size, leading to a more coarsely structured and open lattice network of carbides. This was assumed to have occurred by the dissolution–reprecipitation process of Ostwald ripening. However, these subtle variations were overshadowed by the broad variation in precipitate microstructures within each coating, such that this internal variation was greater than the variation between samples as a function of treatment time. Because of the marked variation precipitate size within each sample, it was not meaningful to quantify the "average" grain size as a function of time.

The rapid transformation from the as-sprayed state with short term heat treatment was, therefore, driven by the metastable nature of the metallic binder phase. Once this driving force had been addressed through carbide precipitation, microstructural development was driven primarily by the surface energy minimization between the phases. The magnitude of this driving force was dramatically lower than that of precipitation at this temperature, accounting for the minimal microstructural developments of the 60 minute time period.

Figure 7 presents the summary images of the coatings treated in the conventional furnace at 5, 10, 30 and 60 minutes. At each exposure time, the furnace-treated sample showed the same microstructural developments are seen in the microwave-treated samples. Again, the variation microstructural development within the furnace-treated sample, due to variations in initial carbide dissolution, was greater than the overall differences between the furnace and microwave-treated samples. Similarly, there were no significant changes in microstructure with increasing treatment time in the furnace trials aside from the same subtle variations in grain growth highlighted in the microwave samples. The change in precipitate size with treatment time is somewhat at odds with the conclusions from the crystallite data from the XRD analysis which implied negligible change in crystallite size after 10 minutes. A contributing factor to this discrepancy was the averaging effect of the XRD analysis over the full spectrum of carbide grains in its analysis, in contrast to the individual carbide precipitates seen visually. Attempts at quantifying the average carbide precipitate size using image analysis proved unsuccessful due to the variation in degree of carbide decomposition throughout the coating prior to heat treatment, together with the complex nature of the precipitate size distribution, morphology and degree of precipitate agglomeration. Because the extent of carbide dissolution varied throughout the coating, it meant that there was not a constant baseline to compare the growth of
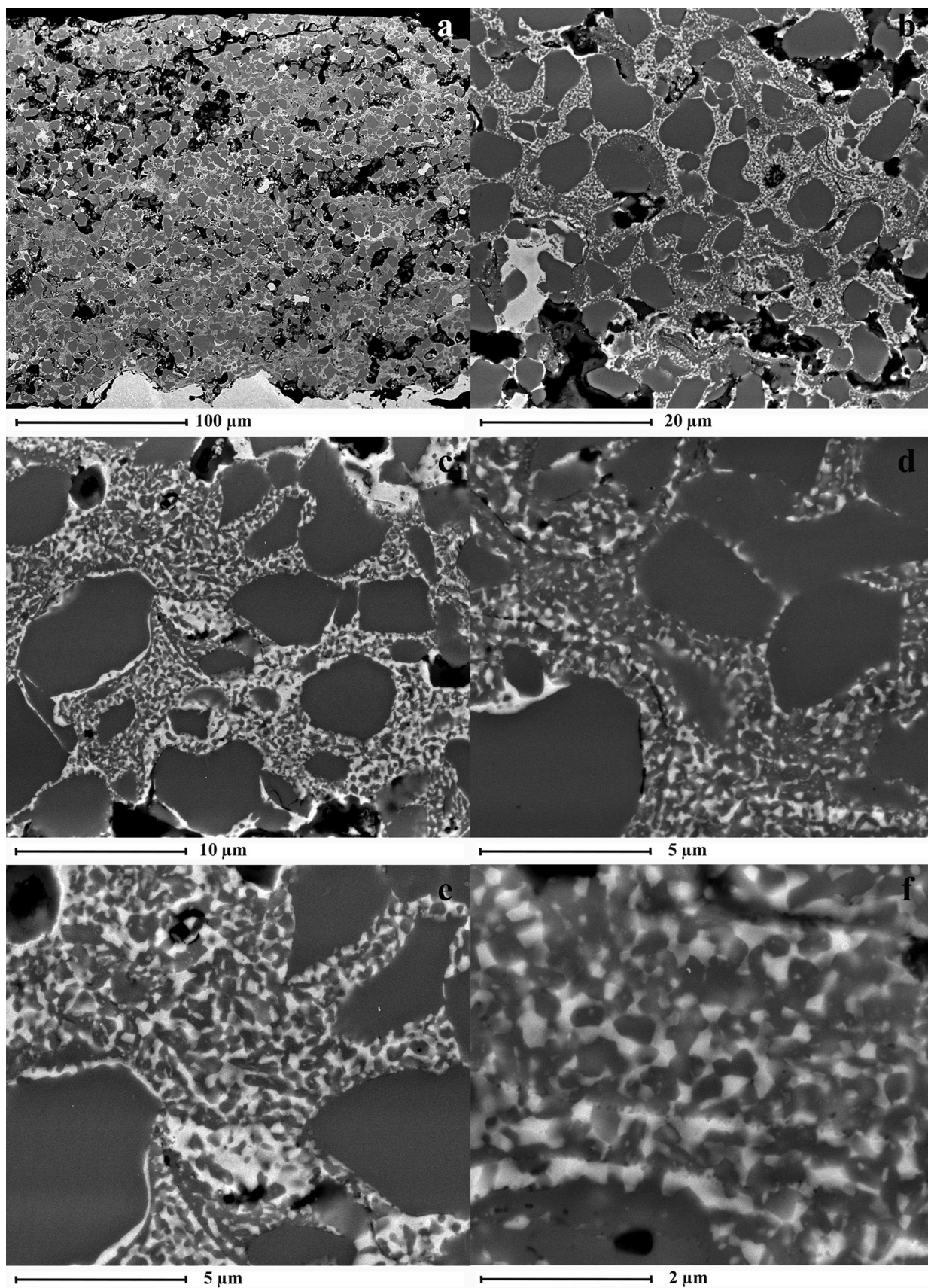
grains in individual splats with increasing treatment time. The significant variation in grains size due to variations in carbide dissolution made the error in the average value so high that it was not possible to make accurate interpretations of the grain growth kinetics. As such, it was not possible to quantify the kinetics of grain growth between the two treatment methods.

WC-Co Coatings—Powder and As-Sprayed Coating Characterization

The agglomerated and sintered powder exhibited a similar spherical morphology to the Cr_3C_2-NiCr powder, with high internal porosity between the coarser grained (1-10 µm) bright contrast WC carbides and the darker contrast metallic Co particles (Ref 24). XRD indicated the presence of WC (ICSD 246149)(82.2 wt.% Rietveld quantification) and Co (ICSD 44989)(17.8 wt.% Rietveld quantification), Fig. 8. Minor peaks of a third phase, postulated to be a Co_xW_yC phase, were too small to accurately identify or quantify.

The as-sprayed coating was notably denser than the Cr_3C_2-NiCr coating, with the isolated pockets of porosity attributed to small, spherical gas bubbles, or larger features indicative of carbide or splat segment pullout, Fig. 9(a). The bright contrast WC grains were clearly visible, even at low magnification, and homogeneously distributed. The surrounding metallic binder typically formed varying shades of mid-gray contrast, indicative of the incorporation of dissolved/decomposed WC elements. Signs of dark contrast (i.e., an alloyed) Co were rarely seen, implying that WC dissolution or peritectic decomposition had occurred in most splats. This was reflected in the reduction in WC content (48.7 vol.% based on image analysis, 59.7 wt.% based on Rietveld analysis), with the remaining material (i.e., incorporating all phases not identified as WC grains) increasing to 50.3 vol.%/40.3 wt.%. At higher magnification it was apparent that the smaller WC grains had preferentially dissolved, with the larger grains exhibiting rounded morphologies indicative of peripheral dissolution, Fig. 9(b) and (c). The metallic binder phase showed localized swirls of grayscale contrast within a generic mid-gray contrast phase. This was thought to indicate localized variations in dissolved carbide elements within a continuous and homogeneous metallic binder of a relatively uniform Co(W,C) alloy composition. Isolated zones of contrast brighter than the WC grains were also

noted, and attributed to the peritectic decomposition of discrete WC grains to form metallic W, Fig. 9.

Figure 8(b) presents the XRD pattern of the as-sprayed coating. A distinctive feature of the pattern was the broad "hump" in the 38-46° region, indicative of the formation of an amorphous or nanocrystalline material. Based on earlier interpretations (Ref 24) this was assumed to represent highly alloyed, rapidly solidified Co material. Attempts at fitting this amorphous/nanocrystalline peak during Rietveld analysis were unsuccessful in that the calculated Co (amorphous/nanocrystalline + crystalline peaks) content greatly exceeded that observed by image analysis. As a compromise the data are fitted as in Fig. 8(c) to largely exclude the amorphous/nanocrystalline material, but on the understanding that the discussion of the quantified compositional results would need to incorporate this material. The quantified XRD composition of the crystalline material was dominated by WC and Co at 65.4 wt.% and 26.8 wt.%, respectively. The change in relative phase concentrations correlated with the evident carbide dissolution noted in the BSE analysis. Furthermore, low concentrations of the degradation phases WC_{1-X} (ICSD 424342)(2.6 wt.%) and W (ICSD 76151)(2.5 wt.%) implied in-flight peritectic decomposition of WC into a "W-rich liquid + carbon" binary phase mixture, which transformed into the metastable phases upon rapid solidification. W_2C (ICSD 77568)(2.8 wt.%) was assumed to have formed from WC dissolution zones in which carbon had diffused away into the surrounding molten Co in flight, to leave a W:C ratio close to 2:1 upon solidification. These "liquid-phase" mechanisms of degradation phase formation make it highly likely that the molten Co became incorporated within this liquid and trapped within the rapidly solidified phase lattices. This composition was broadly consistent with that reported in a previous work, sprayed under HVOF and high-energy plasma conditions (Ref 15). If the microstructure is simplified to WC + (Co + degradation phases), then the normalized Rietveld composition became 65.4 wt.% WC and 34.6 wt.% (Co + degradation phases). When compared with the image analysis results of 59.7 wt.% WC and 40.3 wt.% "Co," it can be seen that the Rietveld quantification underestimates the "Co + degradation phases" component. The difference in these results was attributed to the amorphous/nanocrystalline Co content excluded in the Rietveld quantification.

WC-Co Coatings—Heat Treatment Analysis

XRD Analysis

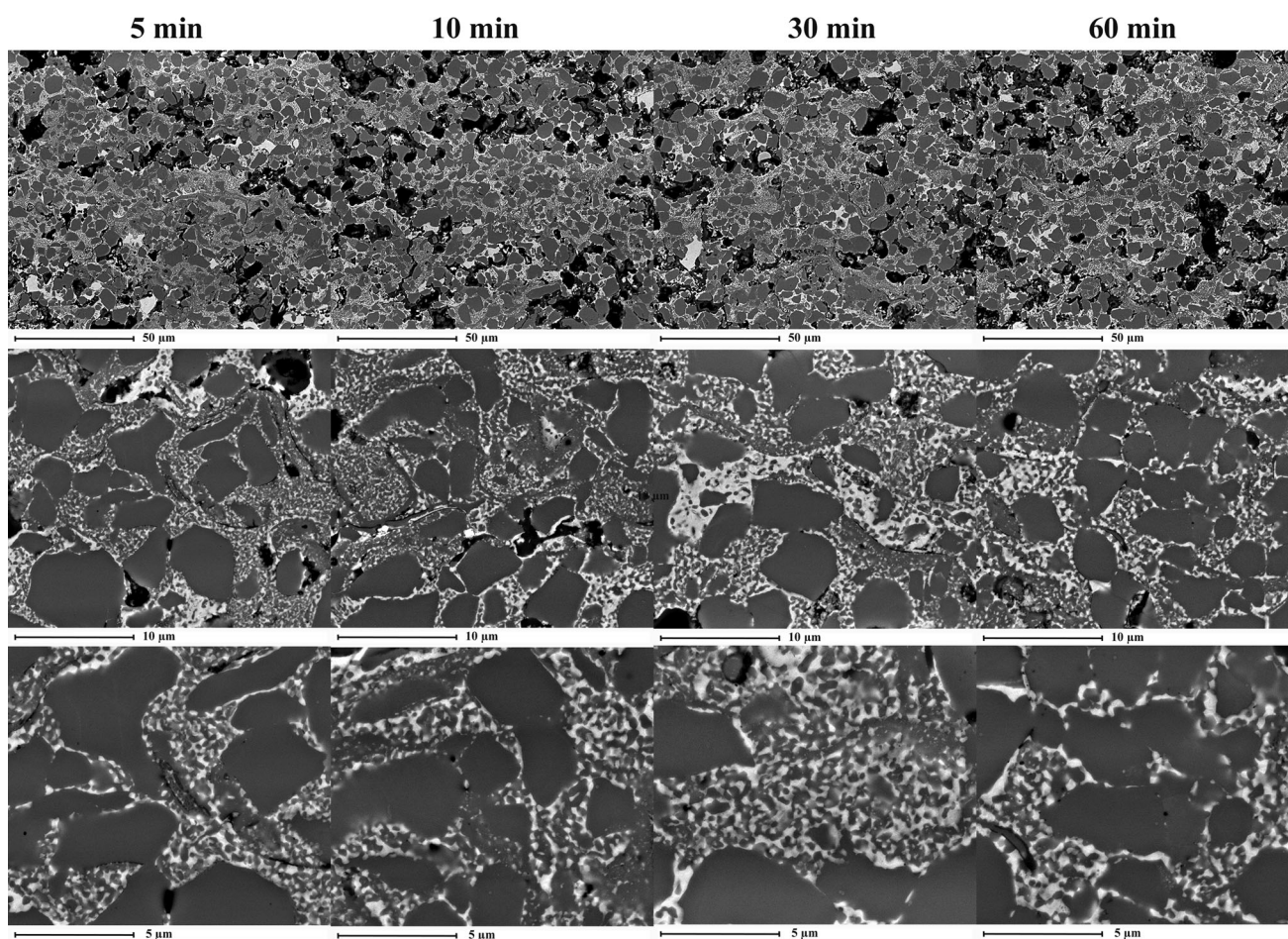Within the first 5 minutes of microwave heat treatment, the as-sprayed coating WC_{1-X}, W_2C and W phases

| 5 min | 10 min | 30 min | 60 min |

Fig. 6 Summary cross-sectional BSE images of the Cr_3C_2-25NiCr coating microwave heat treated for 5, 10, 30 and 60 minutes

disappeared, to be replaced principally by Co_6W_6C (ICSD 198816) with smaller peaks of Co_3W_3C (ICSD 166747), Fig. 10(a) and (b). No other secondary carbide phases or oxides were detected. The postulated amorphous Co peak had fully transformed. The crystalline Co peak had increased in intensity and shifted to a higher 2θ position (lower d-spacing), implying that the dissolved W and C had precipitated out of solution. The rapid transformation of the "degradation" phases WC_{1-X}, W_2C and W implies that these were highly metastable in the as-sprayed coating, and driven to form by a combination of rapid solidification and the localized elemental composition based on the extent of dissolution/decomposition and liquid phase mixing. With increasing heat treatment out to 60 minutes the WC, Co_6W_6C and Co peaks remained constant, while the Co_3W_3C peaks gradually decreased in height to finally disappear in the 60-minute scan, Fig. 10(c).

The 5-minute furnace heat-treated sample showed the same generic developments in the XRD pattern as the microwave-treated sample, but with distinct differences, Fig. 10(d). The microwave pattern was highly crystalline, with well-developed, distinct peaks that were well matched

by the Rietveld pattern fitting, Fig. 10(d). In contrast, the fitting of the furnace-treated sample was notably poorer due to the broad, low intensity nature and lack of peak definition of the metallic Co and Co_3W_3C phases. The Co_3W_3C phase is known to exhibit a broad range of chemistries from Co_2W_4C to Co_4W_2C (Ref 59) which is postulated to account for the poor positional fitting of the secondary Co_3W_3C peak at $\approx 39.5°$. However, in the furnace-treated pattern the main Co_3W_3C peak was ill-defined and very broad, while the secondary peak was more distinct. This raises questions about the validity of the peak identification. An alternative hypothesis postulated that the peak at 39.5° in this pattern was actually residual W_2C material from the as-sprayed coating. In this case, the board peak centered at 42° may be the remnants of the highly alloyed amorphous/nanocrystalline Co material slowly transforming to an equilibrium phase. Both phases in this scenario are postulated based on singular peaks and so are not definitive. Therefore, while the Co_3W_3C phase was fitted, it is acknowledged that the exact composition of these minor phases remains unclear. However, the key difference between the furnace and microwave-treated

samples was that the microwave sample rapidly achieved a highly crystalline composition with narrow peaks, while the furnace-treated sample underwent a much more ill-defined and sluggish transformation, forming distinctly broader and less crystalline peaks at this time, Fig. 10(e). At 10 minutes the furnace-treated XRD pattern showed little difference to that at the 5 minutes with the peaks in question at 39.5° and 42° still ill-defined. At 30 minutes these phases disappeared, leaving only WC, Co_6W_6C and a more well-defined metallic Co pattern. Between 30 minutes and 60 minutes the metallic Co peaks significantly increased in intensity and reduced in width, indicative of a great improvement in the crystallinity of this phase, Fig. 10(f).

The variation in XRD patterns appears to suggest a slightly different mechanistic pathway from the as-sprayed coating to the steady-state coating composition. In the microwave sample, the metastable WC_{1-X}, W_2C and W along with the amorphous/nanocrystalline Co and crystalline Co phases rapidly transformed into a metastable Co_3W_3C phase. The large compositional range for this metastable phase would have enabled the

compositional development to occur locally, while accounting for slight variations in elemental ratios. With time, this metastable Co_3W_3C underwent further transformation to the equilibrium Co_6W_6C phase, with the additional carbon presumably taken up as WC or encapsulated within the Co_6W_6C lattice. The furnace sample underwent a much slower transition from the as-sprayed composition. It is questionable if the Co_3W_3C phase played a significant role in this, or whether the original metastable phases simply transformed directly to Co_6W_6C. The variation in response is postulated to be driven by variations in the diffusion rates of the reacting atoms. One possibility is that the microwave-treated samples transformed faster due to the longer exposure time at high temperature during the heating and cooling periods. However, this is thought to be largely discounted in Fig. 11 which shows that, even after 30 minutes of furnace treatment, the XRD pattern in the region of the $W_2C/Co/Co_3W_3C$ phases is still ill-defined relative to that in the 5-minute microwave-treated sample. The second possibility was that this was a consequence of the variation in thermal heating of the sample between the methods of direct microwave energy transfer and
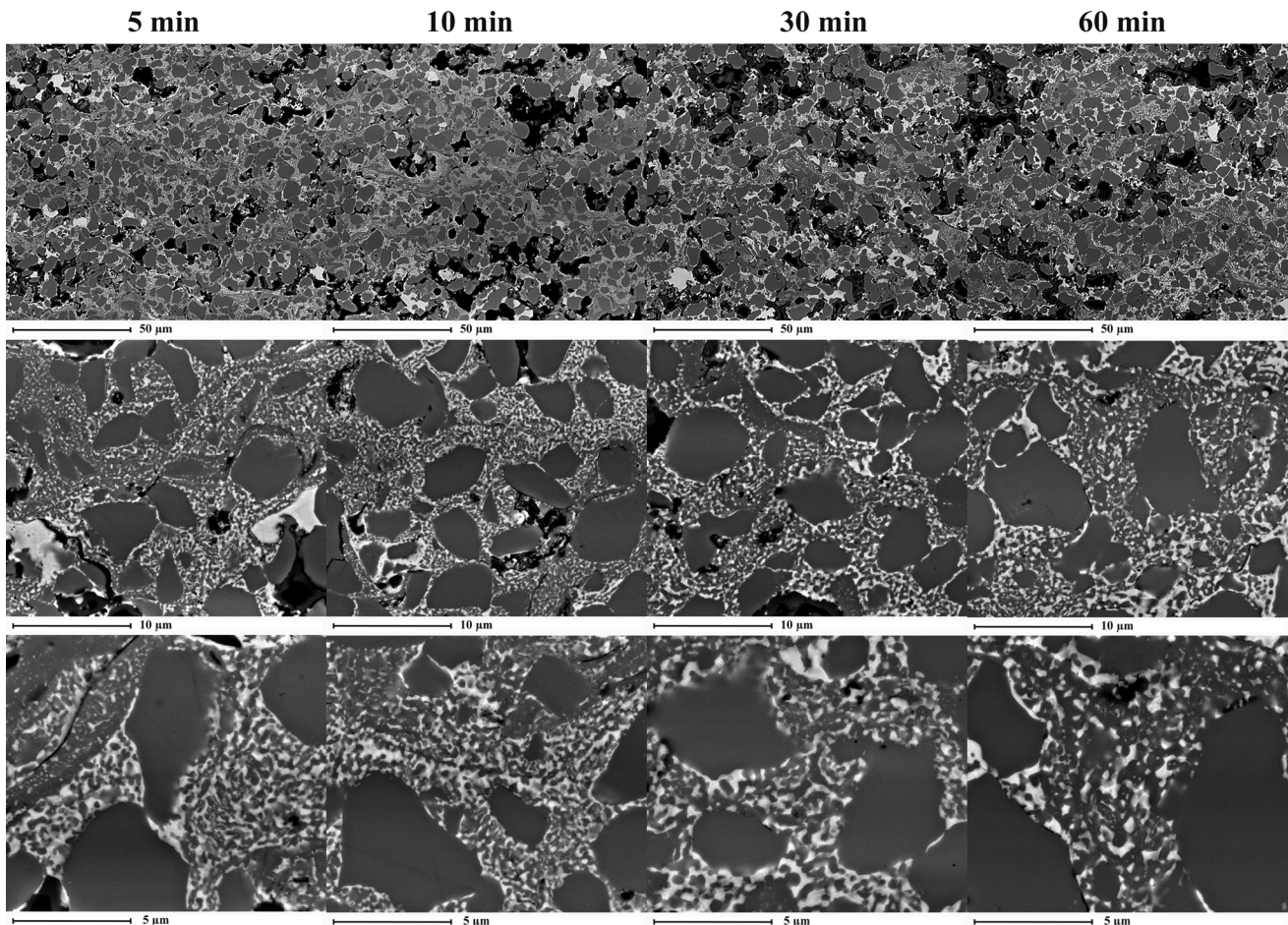

Fig. 7 Summary cross-sectional BSE images of the Cr_3C_2-25NiCr coating furnace heat treated for 5, 10, 30 and 60 minutes
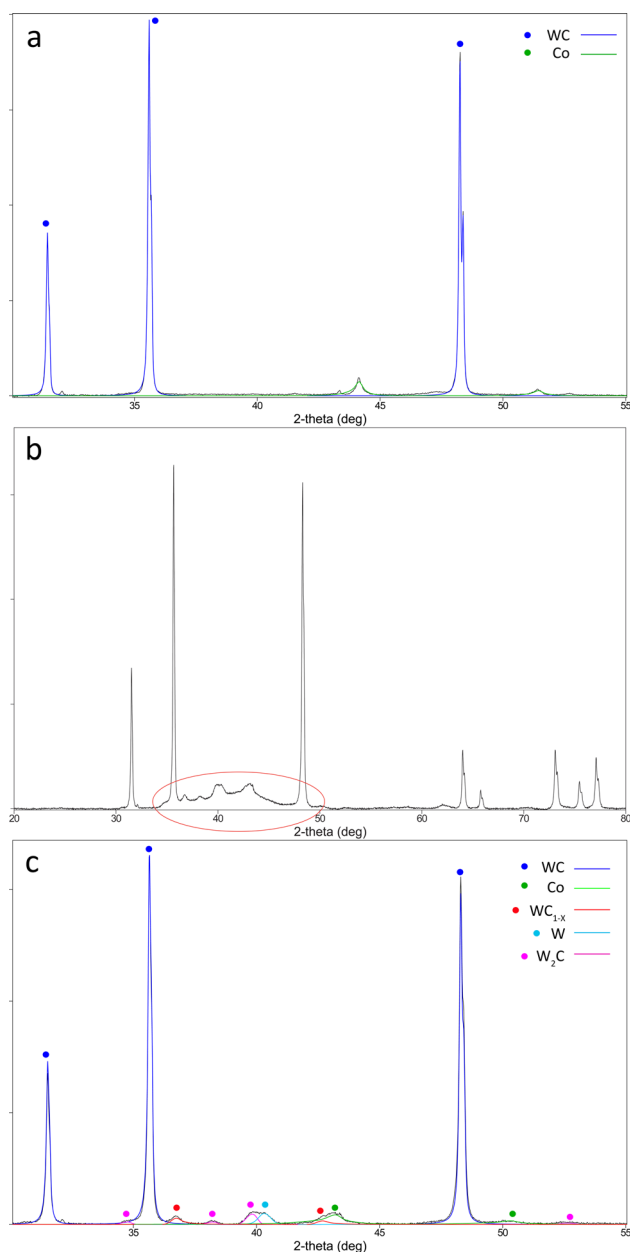
Fig. 8 XRD patterns for the Diamalloy 2005NS WC-17Co powder (a) and the as-sprayed coating (b), with the crystalline phase peaks fitted from Rietveld analysis (c)

the low peak intensity. Furthermore, the coating microstructure is dominated by crystalline stoichiometric carbide compound structures. Diffusion through such structures is expected to be very slow on account of the complex ionic arrangements, especially at such a "modest" temperature relative to the high melting points of these compounds. Fundamentally, there appears to be a difference in the rate and mechanism of atomic rearrangement between these different heating methods in order to account for the observed variation in XRD response with time.

The quantified compositional changes with time based on Rietveld analysis showed the same generic responses for both heat treatment techniques, but with some subtle variations, Fig. 12(a) (Note: the WC and Co concentrations in the as-sprayed coating ($t = 0$) are the raw data, allowing for the concentrations of the metastable WC_{1-X}, W_2C and W phases which are not plotted, and so do not add to 100%). With 5 minutes of heat treatment, the WC and Co concentrations decreased. As the WC content was assumed to reflect the retained WC grains in the as-sprayed coating, which did not change in concentration with heat treatment, this reduction is postulated to reflect the effect of the amorphous Co material which was not accounted for in the as-sprayed coating but which transformed with heat treatment to influence phase concentrations in the treated coating. The reduction in Co concentration reflects the transformation of the highly alloyed Co binder in the as-sprayed coating into a more equilibrium alloy composition, as the dissolved carbide elements precipitated out of solution. The microwave-treated samples effectively reached steady-state after 5 minutes, with only subtle changes occurring up to 60 minutes. The furnace-treated sample showed more overall variation. In particular, it was not until after 10 minutes that the steady-state composition was achieved. Between 5 and 10 minutes the furnace sample WC content decreased, while the Co_6W_6C and Co contents increased. Given that WC is a stoichiometric compound with minimal solubility it is assumed unlikely that the WC phase could transform in such a way as to precipitate the Co_6W_6C and Co phases. Instead, this change is postulated to reflect the continued transformation of any remaining highly alloyed amorphous/nanocrystalline Co material not accounted for in the Rietveld analysis, and in particular that of the ill-defined metastable phases discussed in the XRD analysis.

The 10 to 30 minutes samples remained almost constant for both heat treatment trials. The main variation was the lower Co content in the furnace-treated samples, which accounted for the higher WC and Co_6W_6C concentrations. The reason for this remains unclear but is postulated to relate to the ongoing developments in the Co_XW_YC phases. Over this time the metastable Co_3W_3C phase, which was

unidirectional conduction by furnace treatment, which would further incorporate any additional "microwave-related effects."

Related to this kinetic effect is the physical mechanism accounting for the compositional transformation. In the Cr_3C_2-NiCr structure the metallic binder phase readily enables carbide elements to undergo dissolution, diffusion and re-precipitation to account for potential compositional and microstructural changes. However, in the current coating, the concentration of the metallic Co phase is notably reduced from that in the starting powder based on
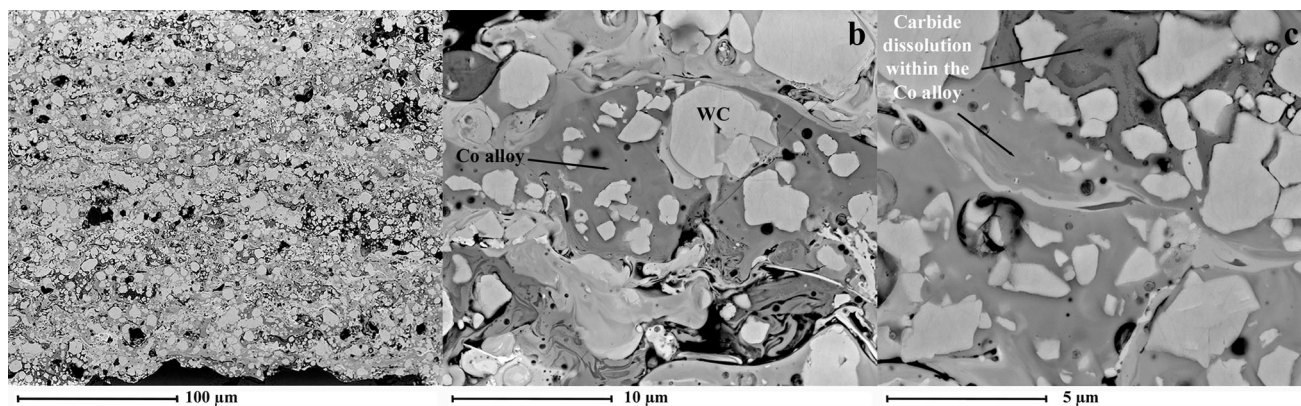
Fig. 9 Cross-sectional BSE images of the WC-17Co as-sprayed coating

already at a low concentration, steadily decreased to be fully transformed in the furnace sample, with less than 1 wt.% remaining in the microwave-treated samples. This was assumed to form the equilibrium Co_6W_6C phase, possibly through reaction was the Co metallic binder material.

From 30 to 60 minutes, the Co_6W_6C content in the microwave-treated sample continued to increase. The reduction in WC and Co concentration suggests that it was the reaction of these phases that accounted for this. In the furnace sample, the metallic Co content dramatically increased in the XRD pattern at 60 minutes, reflecting its increase in concentration at the apparent expense of the Co_6W_6C phase. The WC content remained constant. Co_6W_6C is a stoichiometric/equilibrium phase and so it was not expected to transform in such a way as to generate metallic Co. This remains an area of future work to more deeply understand the thermally induced changes with furnace heating.

After 60 minutes the samples achieved comparable compositions consisting of WC, Co_6W_6C and Co. To put this in context, Fig. 13 presents a vertical section through the Co-W-C system at $X_W:Y_{Co}$ equal to 0.6:0.4 (Ref 60). If no carbon loss occurred, the system should have reformed to an equilibrium Co + WC composition. Any carbon loss pushes the equilibrium composition left such that a 900 °C it should form Co, WC and Co_6W_6C ($M_{12}C$), which matches that observed. The formation and subsequent transformation of Co_3W_3C can be understood also from this carbon-deficient composition, as being rapidly solidified material trapped in its high-temperature structural form during rapid solidification. This then transformed into the equilibrium phases as thermal treatment enabled atomic diffusion to occur.

Figure 12(b) plots the lattice "a" value of the WC phase for the powder and coatings versus the reference value (Ref 61). All values were higher than the reference value. While the powder data may have been influenced by physical

sample height effects, due to the potential settling of the rounded particles, this does not account for the coating data. WC has no solubility for Co and is stoichiometric in regard to carbon (Ref 61). Furthermore, the majority of the WC grains in the coating were retained from the starting powder and did not undergo any obvious changes with the treatment. The larger lattice dimensions cannot, therefore, be justified on a compositional basis. It is possible that this increase reflects a uniform tensile strain on the WC grains, which would be justified in the coating by the change in volume with Co_6W_6C formation discussed in greater detail in the following section. However, further work is required to validate this hypothesis.

Figure 12(c) summarizes the Co lattice "a" value for the powder and coatings, versus the reference value from ICSD 0044 989 for pure Co. Interestingly, the metallic Co remained in the high-temperature FCC form and not the lower temperature ($< \approx 700$ °C) HCP form (Ref 62). The HCP form of Co has negligible W solubility, while in the FCC form it can dissolve a maximum of 15-18 at.% W (data from two different studies in (Ref 63)). The data imply that the metallic Co in the powder was close to pure Co, while the crystalline as-sprayed Co phase was highly alloyed with dissolved W and C from carbide dissolution. With heat treatment, the microwave-treated sample reached a steady-state value distinctly larger than that of the pure Co reference, indicating a stable Co(W) alloy composition. In the furnace-treated sample the Co lattice parameter dropped initially to that of the powder before increasing with treatment time to achieve a value comparable with the microwave-treated sample. This transition in response correlates with the period of ill-defined transformation of the secondary Co_3W_3C phase and the low intensity Co peaks in the XRD pattern, implying they were interrelated in some way. The 60-minute data corresponded to the jump in Co peak definition. The similarity in results at this time implies that this was the steady-state composition. These data again highlight an obvious variation in
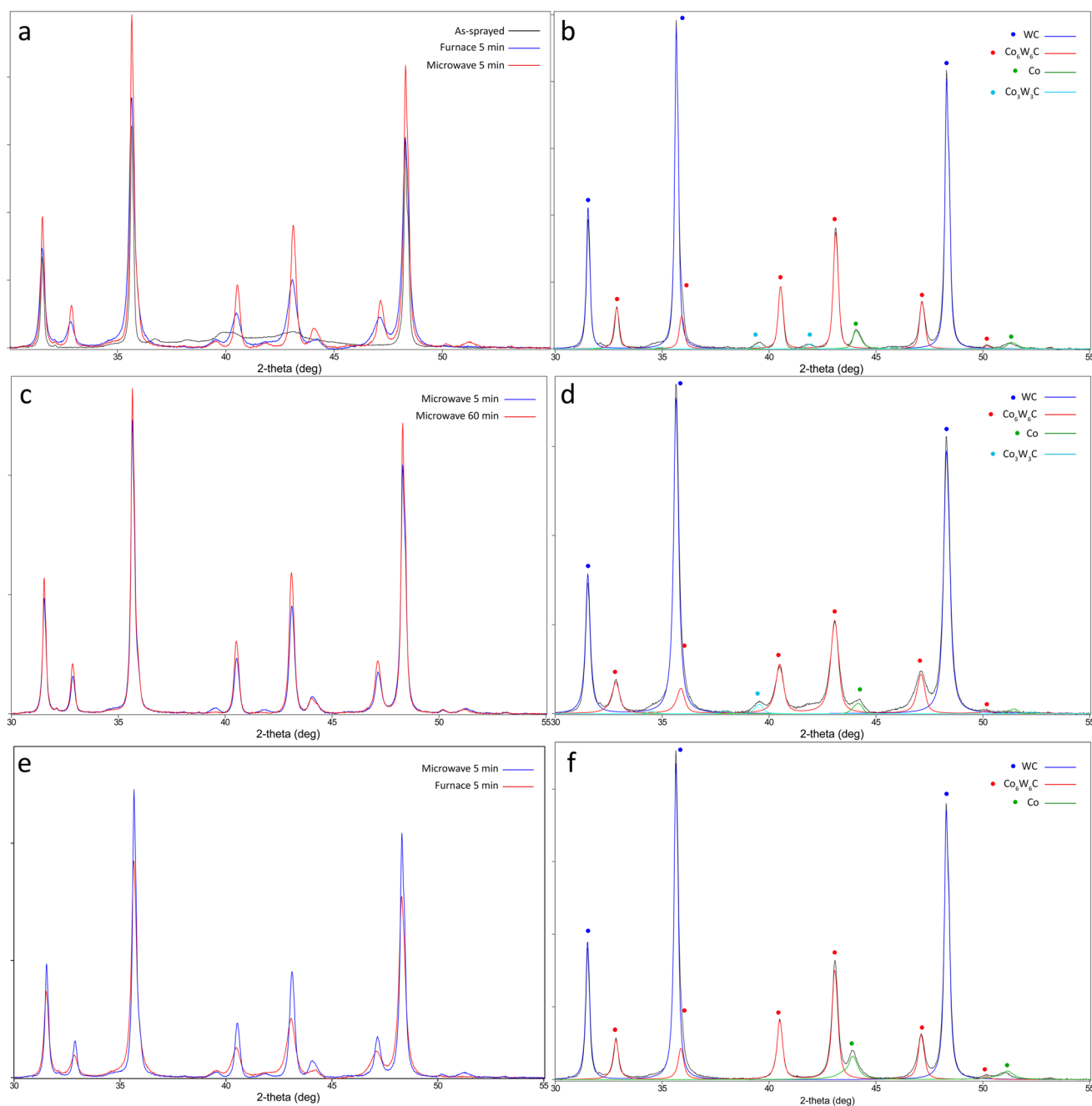
Fig. 10 XRD patterns for microwave and furnace heat-treated WC-17Co coatings – Overlay of the 5-minute microwave and furnace heat-treated samples over the as-sprayed coating (a), the Rietveld fitted pattern of the 5-minute microwave heat-treated coating (b), the overlay of the 60 minute and 5-minute microwave heat-treated coatings (c), the fitted 5-minute furnace heat-treated sample (d), the overlay of the 5-minute microwave and furnace heat-treated coatings (e), and the Rietveld fitted pattern of the 60-minute furnace heat-treated coating (f)

response as a function of each treatment method and reinforce the extremely rapid rate at which the steady-state composition was achieved when using microwave heat treatment.

Figure 12(d) plots the Co_6W_6C "a" lattice parameter for the coatings versus the reference value (Ref 64). As for the WC, the lattice parameters for this phase were distinctly larger than the reference. This phase is very stoichiometric such that compositional changes are not thought to account for such lattice distortions. Instead, it is postulated that the increase in dimensions is again the result of residual tensile stresses within these grains.

Fig. 11 Overlay of the XRD patterns from the microwave 5-minute heat treatment and 30-minute furnace heat treatment, highlighting the notable variation in peak widths, and, therefore, phase crystallinity
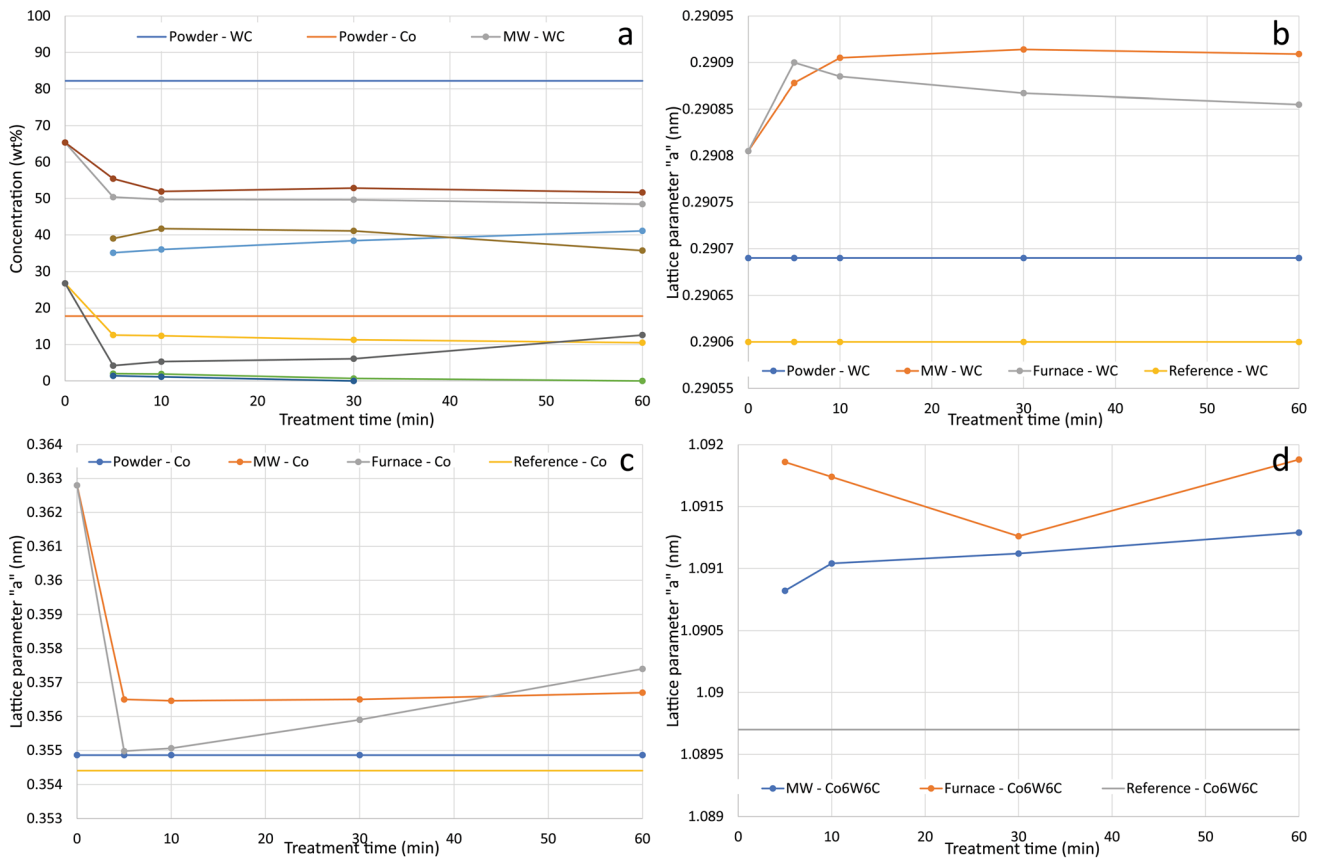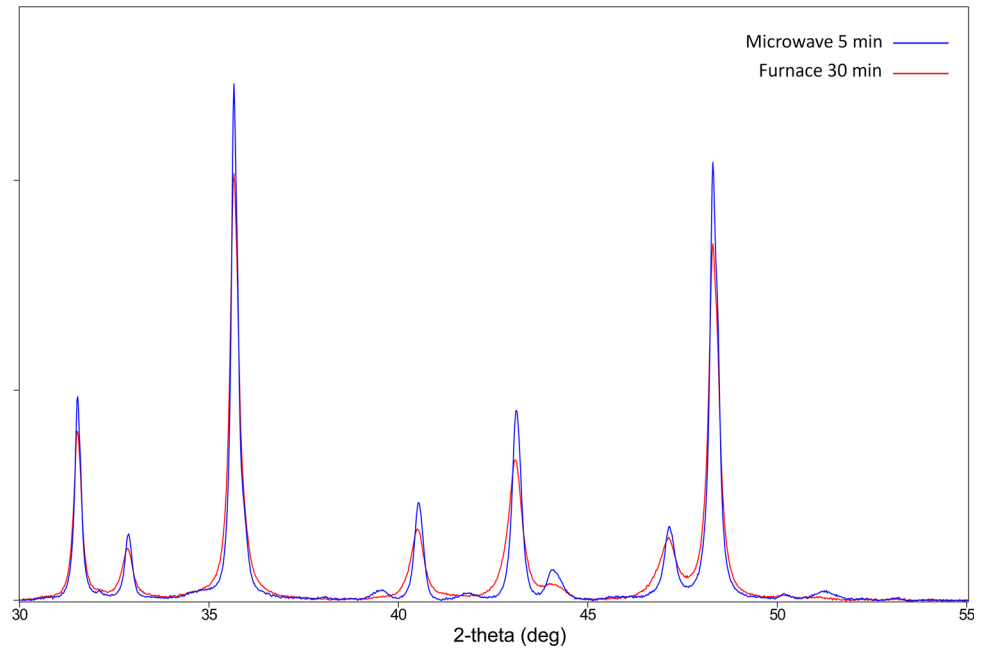

Fig. 12 Rietveld quantified composition of the WC-17Co coatings as a function of microwave and furnace heat treatment time (a), together with the "*a*" lattice parameters for the WC carbide (b), Co alloy (c) and Co_6W_6C (d) phases

SEM Analysis

At 5 minutes of microwave heat treatment, low magnification images showed no differences in the bulk coating microstructure from the as-sprayed state, aside from an increase in "pullout" porosity features, Fig. 14(a). However, at higher magnifications, it was clear that all of the flat, uniform contrast, Co-rich carbide dissolution zones in the as-sprayed coating had transformed into a highly porous, two phase matrix composed of a bright contrast acicular or platelet phase incorporating a much darker contrast phase. The retained WC grains were clearly seen and had acted as preferential sites for precipitation based on the needle-like growth that had developed out from the surfaces. The third class of microstructural features were the bright contrast phases with very fluid morphologies typifying quenched liquid. These were retained from the as-sprayed coating but had undergone subtle changes. In some cases bright contrast elongated needles had precipitated within the solid zones, which were postulated to be WC precipitates. These features were consistent with previous works characterizing the phase microstructure development of WC-Co thermal spray coatings with heat treatment (Ref 24). In that work, the transformed phases of

acicular/platelet material, together with a flat, dense material with fluid morphologies, were postulated to be mixed Co_XW_YC phases (Co_3W_3C, Co_6W_6C or Co_2W_4C). The same mechanisms of microstructural development are believed to have occurred here.

Continued microwave heat treatment out to 60 minutes led to no significant changes in the microstructural morphology or size of the respective features, Fig. 15. The lack of significant microstructural development was attributed to the same scenario as discussed for the Cr_3C_2-NiCr coatings. Development was inhibited further by the highly crystalline compound nature of the precipitated phases, without the continuous metallic binder phase to promote diffusion-based mechanisms of grain growth.

Figure 16 presents the summary images of the coatings treated in the conventional furnace at 5, 10, 30 and 60 minutes. As noted in the Cr_3C_2-NiCr coatings, the furnace-treated sample showed the same microstructural developments as seen at each exposure time in the microwave-treated samples. Variations in morphology within each coating were, again, greater than the variations in morphologies between the coatings.

The formation of Co_6W_6C with heat treatment from the highly alloyed Co alloy formed from carbide dissolution


Fig. 13 Binary WC-Co plane through the Co-W-C ternary phase diagram highlighting the powder composition and potential phase developments with a loss of carbon. Reproduced from (Ref 60)
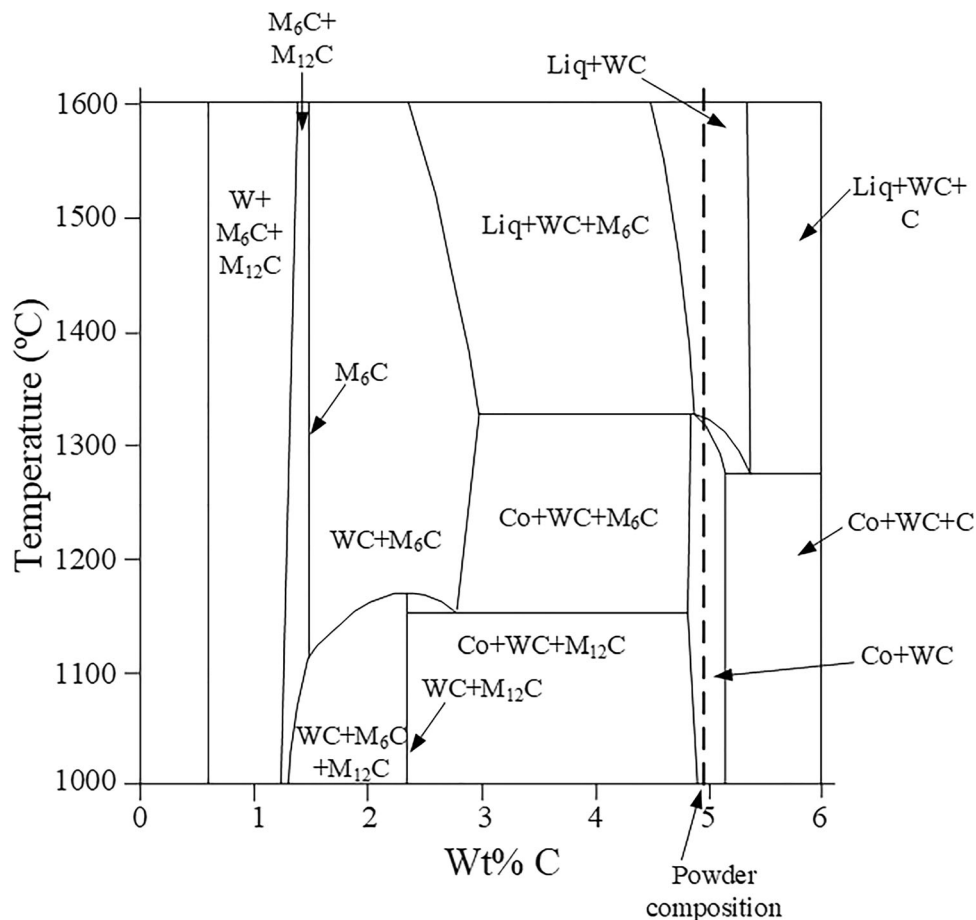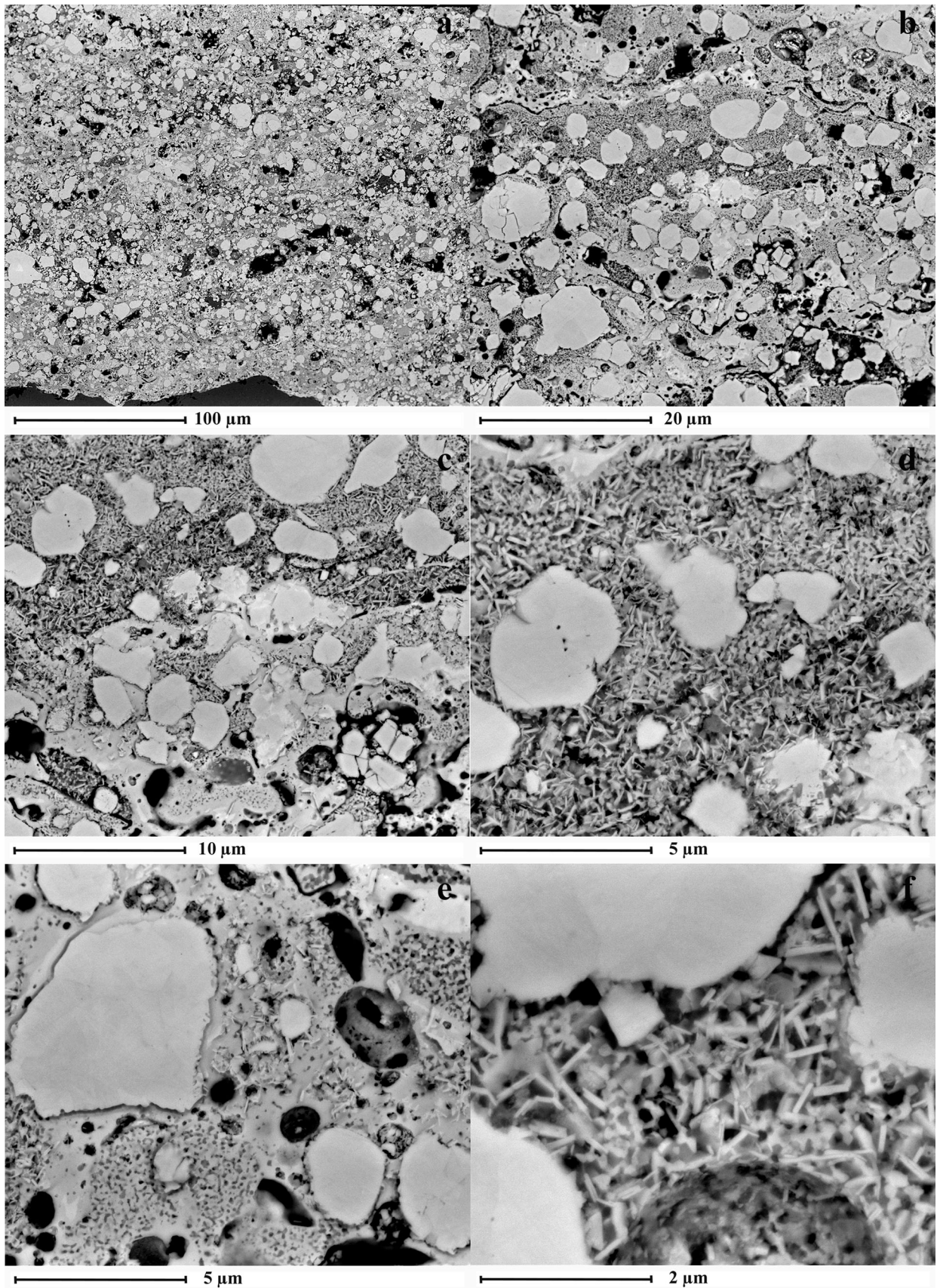
◄ **Fig. 14** Cross-sectional BSE images of the WC-17Co coating microwave heat treated for 5 minutes

was postulated to account for the porous nature of the microstructure. Two mechanisms are considered to give rough approximations of the possible volume changes:

$$6WC + 6Co \rightarrow Co_6W_6C + 5C \qquad \text{(Eq 1)}$$

$$6W + 6Co \rightarrow Co_6W_6C \qquad \text{(Eq 2)}$$
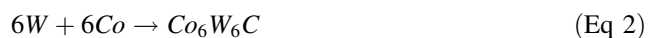
In mechanism 1 the volume of the highly alloyed Co from which the Co_6W_6C precipitated is approximated to be the same as the starting constituents. The excess carbon is assumed to be lost as CO_2 or to have diffused elsewhere in the microstructure. The change in volume from the reactants to the Co_6W_6C form is − 14.9%, a notable reduction in volume. In mechanism 2, it is assumed that the excess carbon is lost in-flight such that the highly alloyed Co in the as-sprayed coating consists only of the elements required to form Co_6W_6C. If the density of this metastable alloy is assumed to follow a simple rule of mixtures, then the change in volume is − 4.5%, a small reduction. More detailed data are required to more accurately describe this, but this first approximation serves to justify, in principle, that the reduction in volume can result in formation of porosity. This reduction in volume would also tend to generate a tensile stress in the retained carbide grains, potentially accounting for the shift in lattice parameter highlighted above.

Vickers Microhardness

Figure 17(a) plots the Cr_3C_2-NiCr coating Vickers hardness values (VHN$_{200}$) is a function of time for both the treatment methods. The hardness of the dense regions of the Cr_3C_2-NiCr coatings under a 200 g load was comparable with those presented for conventional Cr_3C_2-NiCr coatings deposited by various techniques (Ref 16, 65). In this case, the solid solution strengthening of the ductile NiCr leads to an increase in strength of the binder phase, contributing to the overall hardness (Ref 65). With heat treatment the average hardness dropped to a steady-state level of ≈900 VHN$_{200}$ and remained constant out to 60 minutes for both techniques. The reduction in hardness is the direct result of carbide precipitation, reducing the magnitude of Ni binder strengthening. The same effect was seen in longer-term trials out to 5 days treatment at this temperature (Ref 65). In that work, the short-term hardness response was attributed to the compositional changes in the binder with carbide precipitation. Gradually the hardness recovered with extended treatment due to a combination of the formation of interconnected carbide networks, and the

sintering of the splat boundaries with reduced splat-splat sliding under load. While the compositional recovery mechanism had occurred in this work, there was insufficient time for the formation of interconnected carbide networks. However, what this result also indicates is that neither heat treatment technique generated sufficient splat–splat bonding to increase the microstructural component of the coating hardness.

Figure 17(b) plots the Vickers hardness values (VHN$_{200}$) for the WC-Co coatings. The as-sprayed hardness of the dense regions was at the lower end of values typically presented in the literature (Ref 66, 67). Heat treatment also led to a drop in hardness to a steady-state value of ≈800 VHN$_{200}$. This is very low for this coating composition. In this instance, it was the formation of the porous microstructure with heat treatment that led to the consistently low hardness results.

Discussion

Comparison of Microwave Versus Thermal Heating as a function of Coating Composition

Heat treatment of both coating compositions, by both microwave and conventional furnaces at 900 °C, led to the rapid transformation of the metastable as-sprayed coating compositions and microstructures to steady-state compositions within the first 5 minutes. The Cr_3C_2-NiCr coatings were comparable between the heat treatment methods across all compositional, phase and microstructural analysis. Similarly, the WC-Co coatings were comparable across the analysis, with the exception that the microwave-treated sample XRD patterns were notably more crystalline from a much earlier treatment time compared to the furnace-treated samples. To account for these observations in terms of the original aims of this work, the following aspects are discussed:

- Material properties and their potential effect on the interaction with microwaves
- The physical coating microstructure interaction with microwaves
- The critical phase transition temperatures as a function of coating composition

Material Property Effects on the Interaction with Microwaves

The interaction of materials with microwaves is critically dependent on a vast number of electromagnetic properties, much more than thermal conduction (Ref 25-30). The variation in material properties affects the mechanism of

the microwave–material interaction and subsequent heating, and it is, therefore, of interest to contrast these properties between the Cr_3C_2-NiCr and WC-Co systems to determine if these can account for the observed responses. Table 3 summarizes some of the key thermal and electromechanical properties of these materials. It is notable that the majority of material properties required to describe the fundamental interaction of microwaves with materials (Ref 68) are not included, simply because this information was not available. Moreover, even for those properties that were reported, there is significant variation in response with changes in composition by alloying, doping or impurities, crystal structure and morphology/size, for a given nominal material. A prime example of this being that equilibrium Co has a HCP crystal structure at ambient temperature, yet the Co matrix in this work retained an FCC structure for which little material property data have been reported. While this precludes a quantitative comparison on the basis of the fundamental microwave interaction formally, it is informative to qualitatively contrast the two material systems.

The thermal conductivity of the carbide phases is notably higher than that of the metallic binders in both systems, Table 3. This is particularly significant in the Ni(Cr) binder where the addition of Cr dramatically reduces the conductivity compared to pure Ni. A similar effect occurs in Co with increasing levels of W alloying (Ref 69). These phenomena are particularly relevant here as the as-sprayed coatings both exhibited high degrees of carbide dissolution, resulting in extremely high degrees of alloying of the metallic phase. In principle, any beneficial effects of microwave processing in terms of internal or volumetric heating relative to one-directional thermal conductivity would be expected to overcome the poor thermal conductivity of the highly alloyed metallic binders and generator faster phase transition to equilibrium. This was not observed in the Cr_3C_2-NiCr system, but could have contributed to the slower transition of the WC phase development in the furnace-treated WC-Co system, Fig. 12(a), and the greater degree of crystallinity seen from the earliest microwave heat treatment time compared to the slower crystallinity development in the furnace-treated WC-Co samples.

The electrical resistivity of the WC-Co phases is notably lower than that of the Cr_3C_2-NiCr phases, particularly the Ni(Cr) alloy, Table 3. However, in drawing similarities with the changing conductivity of Ni with Cr alloying, it is possible that the electrical conductivity of Co may be influenced by high degrees of W alloying. When taken at face value, the higher resistivity of the phases in the Cr_3C_2-NiCr system would be expected to generate a greater heating effect due to electrical resistance during interaction with the electric field component of the microwaves

compared to the WC-Co system. This should result in faster heating rates and faster phase developments during microwave processing relative to purely thermal processing.

Few magnetic properties of the system phases were reported in the literature, with only the simplest of magnetic responses found. It is notable that the two systems exhibit opposite trends. In the Cr_3C_2-NiCr system the carbide is ferromagnetic (Note: the ferromagnetic response has been reported for 2D MXene Cr_3C_2 phases (Ref 70) and nanoplatelets (Ref 71, 72). The translation of this 2D response to bulk 3D structures is unknown). In contrast, the Ni(Cr) alloy is non-magnetic, assuming that the highly alloyed Ni phase exhibits properties indicative of "Nichrome" wire and not those of pure Ni which is ferromagnetic. In contrast, WC (and notably the degradation phase W_2C and potentially Co_2W_4C, based on analogy with the Ni_2W_4C phase (Ref 73)) is non-magnetic, while Co is ferromagnetic. The mechanism of response to the magnetic field component of the microwave would, therefore, be expected to differ significantly between the systems. Given the critical nature of the binder in the precipitation of dissolved species seen in this work, the WC-Co system would be expected to benefit the most from this magnetic field interaction. This discussion is based on theoretical considerations of the fundamental postulated mechanisms of the magnetic field interactions with materials. However, experimental work indicates that the situation is more complex than considered to date. Cheng et al (Ref 36) contrasted the heating rates of materials in high electric field-based microwave fields and high magnetic field-based microwave fields. Cobalt powder compacts showed a much higher heating rate and peak temperature when heated in the magnetic field based trial, which is consistent with the postulated theory above. However, the WC powder compact was also heated at a much higher rate and to a higher peak temperature in the magnetic field-based trial compared to the electric field trial. This contradicts the theoretical assumptions made above, highlighting the postulated theories are incomplete in accounting for the magnetic field effects of microwave interactions.

Given the high temperature of processing it is prudent to also consider the materials Curie temperatures. However, in the context of this work, this was only relevant for Co, given that WC and Ni(Cr) are non-magnetic and no data were available for Cr_3C_2. Cobalt's Curie temperature is 1131 °C, well above the processing temperature used here and implying that magnetic field effects would still be relevant under these test conditions. It is notable that the HCP to FCC phase transition occurs at 422 °C, implying that the FCC phase seen in this work would still be responsive to the same magnetic field effects as seen in
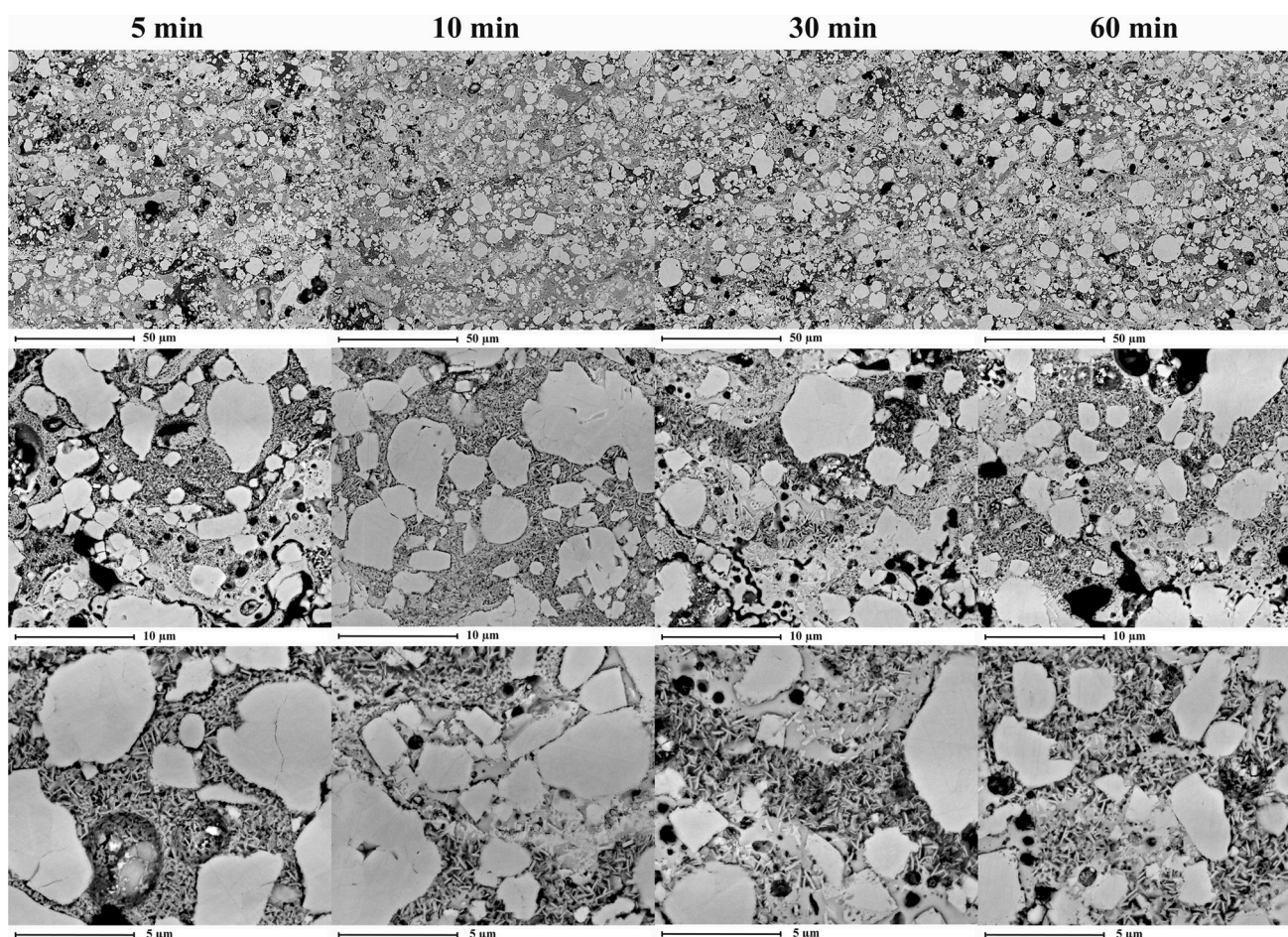
5 min	10 min	30 min	60 min

Fig. 15 Summary cross-sectional BSE images of the WC-17Co coating microwave heat treated for 5, 10, 30 and 60 minutes

conventional HCP-Co based WC-Co composites treated at lower temperatures.

Physical Coating Microstructure interaction with Microwaves

Table 3 highlights that the penetration or "skin" depth of microwave interaction with bulk component materials (Note: No information could be found for the penetration depth of Cr_3C_2). However, as highlighted in the literature (Ref 26, 27) when these materials are in powder form they can be effectively processed by microwave treatment to high/full density to depths of up to at least 50 mm (Ref 28, 36). A common proviso to microwave processing of metal powders is that the particle size had to be less than or equal to the penetration depth of the material in order for the powdered metal to couple directly with the microwaves (Ref 26)—in this case implying particles < 2.5 μm for the metallic phases and < 4.5 μm for WC. However, work by Saitou (Ref 29) highlighted that compacts of metallic powders averaging from 5 μm (Co), to < 45 μm (Ni and 316L stainless steel), up to < 75 μm (Cu powder), and

pellets of 12 mm diameter and 7-10 mm thick (relative density 58-73%) could be sintered to near full density. Faster particle sintering was observed for smaller particles. The ability of such "large" particles, well in excess of the skin depth, to reach the temperatures required to achieve full density implies that this "particle size effect" is perhaps of secondary rather than primary importance.

The translation of trials on compacted powders to thermal spray coatings has many similarities, but also distinct and important differences. Thermal spray coatings are comprised of individual "splats" which are, for the most part, mechanically bound and interlocked with those around them, i.e., the microstructure is made up of discrete "units" physically packed together, in a similar manner to a powder compact. The thickness of each splat was typically less than 10-12 μm. Each interface is delineated by a physical separation between the splats from either a microscopic airgap at the splat boundary and/or an inter-splat oxide layer. Within the splats, the average carbide size was 6.5 μm for Cr_3C_2 and 4.1 μm with WC, with the dimensions of the continuous metallic binder between these being less than 10 μm in extreme cases and averaging
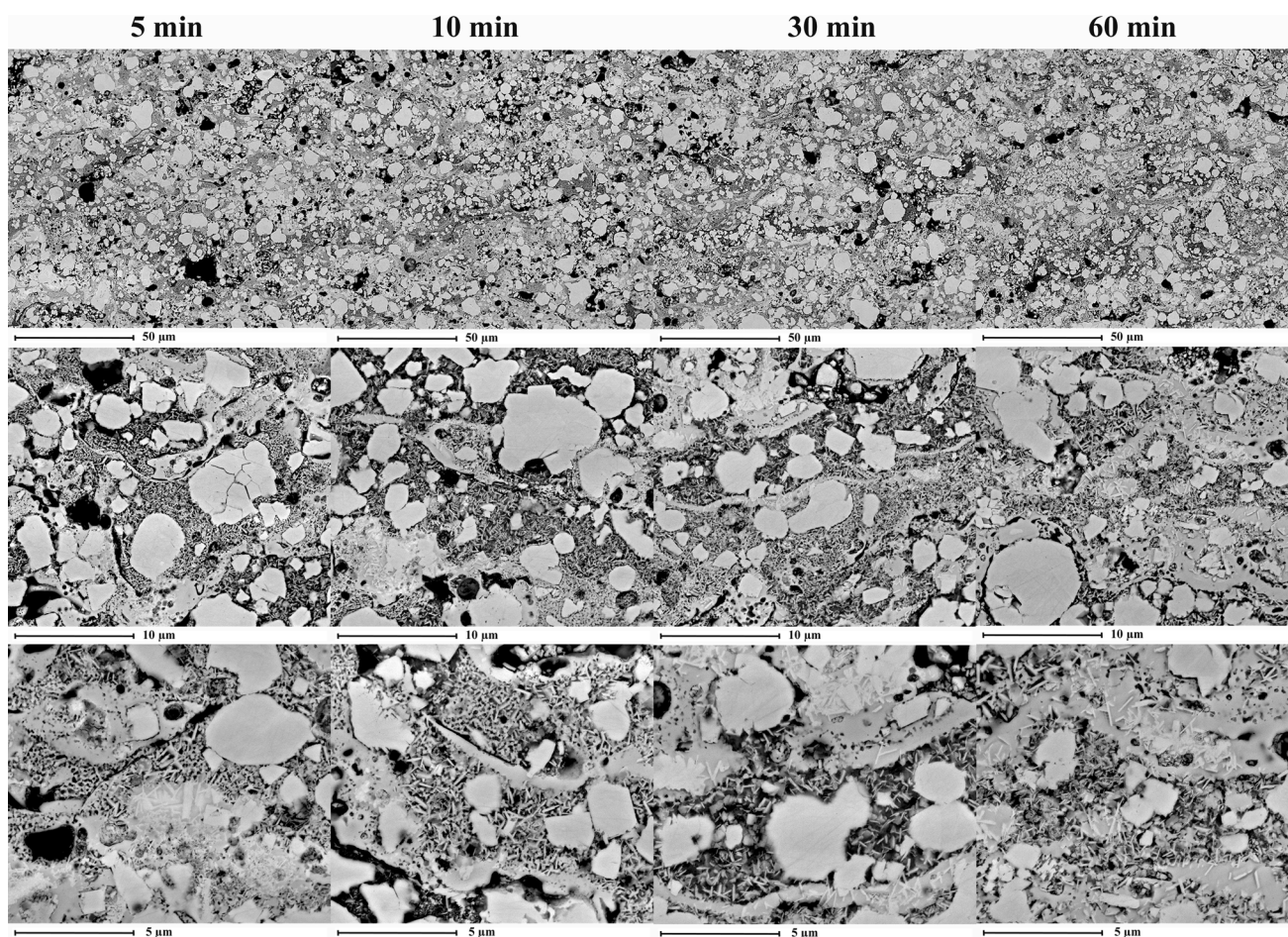
Fig. 16 Summary cross-sectional BSE images of the WC-17Co coating furnace heat treated for 5, 10, 30 and 60 minutes

less than 2-5 μm in most instances. The porosity volume was notably lower, while the morphology and distribution of this porosity also differed from that in typical powder compacts. The results of this work show the thermal spray coatings can be successfully treated by microwave heating. While it is tempting to draw similarities in terms of results with those of Saitou (Ref 29), the translation of mechanisms accounting for these results remains unclear. A complicating factor is that the limited work applying microwave heating to thermal spray coatings (namely those of (Ref 45, 50) and this work) both use the "hybrid" processing approach, incorporating susceptors to generate radiant thermal heating as well as microwave interaction. To the best of our knowledge, no works have trialed microwave-only heating to establish the response of the coating structure under only electromagnetic stimulation. This is an obvious area requiring further research.

Critical Phase Transition Temperatures

The test temperature of 900 °C was selected to exceed the critical transition temperatures in plasma-sprayed Cr_3C_2-NiCr and WC-Co coatings published in the literature (Ref 24, 52, 74-76). These were 735-800 °C and 830 °C, respectively, for the transformation of the supersaturated metallic binder phases to form equilibrium compositions of alloy phases with carbide precipitates.

For the Cr_3C_2-NiCr coating in the current work, the variation in plasma parameters, from those referenced above, to generate a lower temperature, higher velocity plasma plume resulted in less heating of the particles, as evident in the more porous microstructure compared to that in the literature (Ref 52). As such, the extent of carbide degradation was dramatically reduced, with only carbide dissolution occurring to yield retained Cr_3C_2, a crystalline Ni(Cr) alloy and an amorphous/nanocrystalline Ni(Cr) alloy. Based on this composition, full recovery to the equilibrium $Cr_3C_2 + Ni(Cr)$ alloy composition would occur at temperatures up to only 620 °C. Treatment at 900 °C was high enough that any bespoke phase/microstructure developments induced by microwave treatment would have been overshadowed by the high thermal driving force. This is postulated to be the primary reason for the lack of significant differences between the

Fig. 17 Vickers microhardness (VHN$_{200}$) of the Cr$_3$C$_2$-NiCr (a) and WC-17Co (b) coatings as a function of microwave and furnace heat treatment time
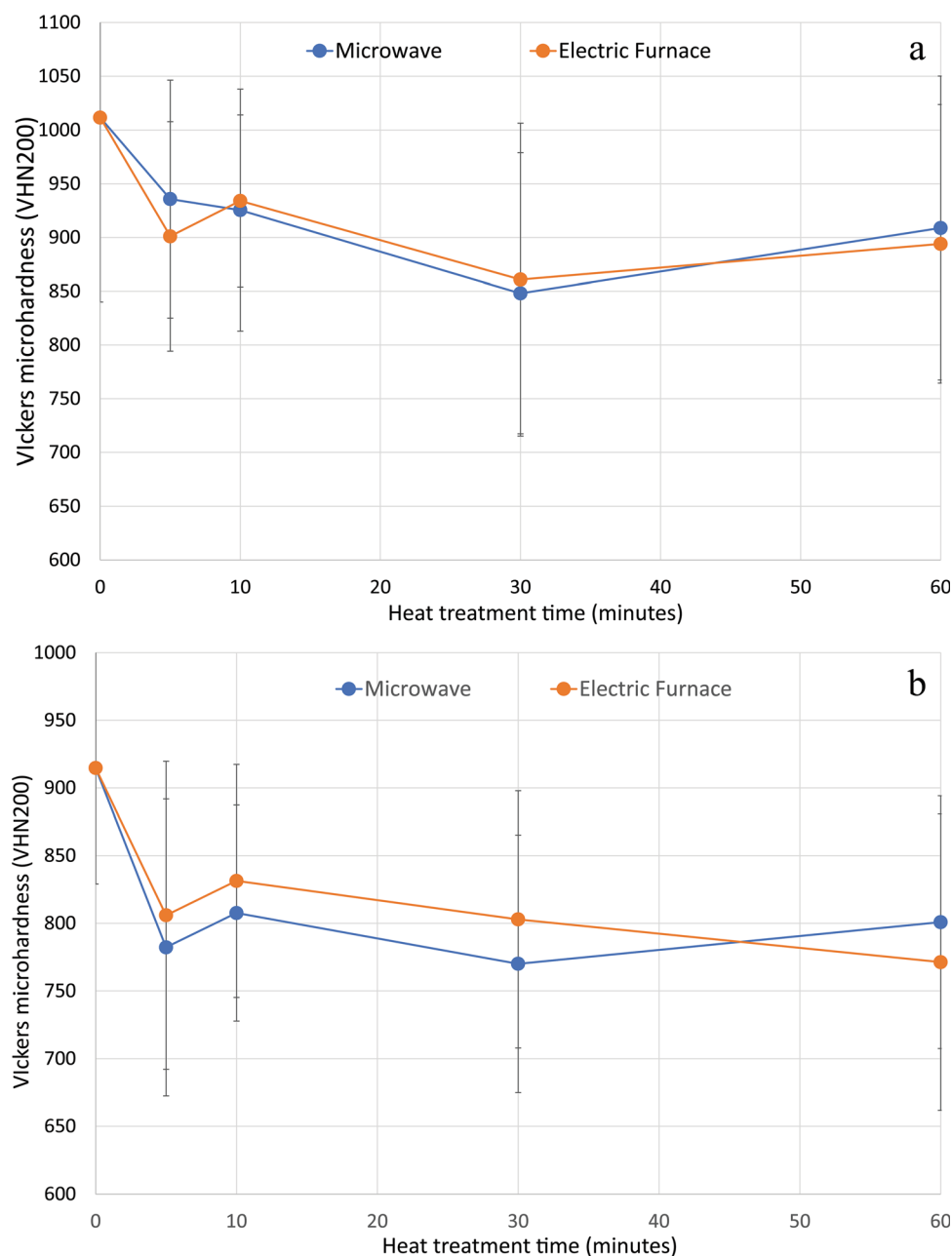
microwave and furnace-treated samples. To better assess the potential of microwave treatment, future work is recommended to consider denser coatings, and trial short exposure periods below and above the critical temperatures highlighted in the literature to better highlight the potential kinetic effects of microwave treatment.

As in the previous coating, the plasma parameters of this work led to significantly lower concentrations of the carbide decomposition phases WC$_{1-X}$, W$_2$C and W compared to the literature (Ref 24), with the composition dominated by retained WC and a Co alloy. Based on this composition, recovery to the equilibrium composition of WC, Co and Co$_6$W$_6$C could have been achieved at 750-800 °C.

Therefore, there is again an extreme thermal driving force that potentially overcame the benefits of microwave treatment. However, in this case, it was notable that the microwave sample showed a much higher degree of crystallinity from the earliest treatment time of 5 minutes, while the same degree of crystallinity in terms of narrow peak width was not seen in the furnace-treated samples until after much longer treatment times. Increased crystallinity implies greater atom mobility and diffusion to lead to grain growth. Such atomic-scale rearrangements in the WC-Co system are complicated by the extremely large size of the tungsten atom relative to those of cobalt and carbon. These results infer that microwave treatment led to an

Table 3 Summary of material property data

	Cr_3C_2	Ni(Cr)	WC	Co
Thermal conductivity, W/(m.K)	189.77 (Ref 77, 78)	Ni @25 °C 90.7 (Ref 77) @1127 °C 80.4 (Ref 77) Ni20Cr @25-700 °C 12-23 (Ref 77) Nichrome 8-17 (Ref 79)	110 (Ref 80) 155 (Ref 69)	100 (Ref 77) 69.21 (Ref 81) 67.2 (Ref 69) NOTE: Thermal conductivity of Co decreases with addition of large atoms, such as W (Ref 69).
Electrical resistivity, $\Omega.m$	75×10^{-8} (Ref 82)	Ni $7\text{-}10 \times 10^{-8}$ (Ref 83-85) Nichrome $100\text{-}150 \times 10^{-8}$ (Ref 79)	20×10^{-8} (Ref 82)	5.6×10^{-8} (Ref 83, 85)
Magnetic properties	Ferromagnetic when in the form of 2D layered MXene compound (Ref 70, 86) and nanoplatelets (Ref 71, 72). No information found for bulk Cr_3C_2.	Ni ferromagnetic (Ref 87) Nichrome nonmagnetic (Ref 88) Curie temperature 358 °C (Ref 89)	WC nonmagnetic (Ref 73) W_2C nonmagnetic (Ref 73) Ni_2W_4C nonmagnetic (Ref 73) Ni_3Mo_3C is weakly magnetic. Response strongly correlated with 3d electrons in Ni (Ref 73). As Co has a similar structure and properties as Ni, it is possible that this behavior also applies to Co_3W_3C. WC-Co ferromagnetic (Ref 90), equivalent to that of bulk Co.	Ferromagnetic (Ref 91) Curie temperature 1131 °C (Ref 87)
Microwave penetration		Ni 2.5 µm (Ref 68)	WC 4.7 µm (Ref 41) However, WC-6Co green powder metallurgy parts (powder particle size 1 µm) have penetration depths of 75 mm (Ref 41)	Co 2.5 µm (Ref 41, 68)

increase in atomic mobility over that seen in the furnace-treated sample. However, the mechanism accounting for this, such as a higher internal sample temperature versus external temperature (Ref 27) or a fundamental "microwave effect" (Ref 26, 27), requires further research to define.

Conclusions

This work explored the novel application of microwave heat treatment to thermally sprayed Cr_3C_2-25wt.%Ni(Cr) and WC-17wt.%Co composite coatings to generate nano-carbide-reinforced coating microstructures. The rate of phase development was contrasted with conventional furnace heat treatment. The main conclusions from this work were:

- Both compositions were successfully heat-treated using microwave heating, with support from susceptors.
- The Cr_3C_2-NiCr coatings transformed into equilibrium Cr_3C_2 and Ni(Cr) alloy compositions with approximately 10 wt.% Cr_2O_3, within the first 5 minutes of heat treatment by both microwave and conventional furnace heating. The compositional and microstructural results closely matched for both heating methods out to 60 minutes, with the variation within each sample greater than the variation between the heat treatment methods.
- The WC-Co by both heat treatment techniques formed compositions dominated by WC and Co_6W_6C, with minor amounts of a Co alloy and Co_3W_3C. While the microwave-treated samples completely transformed in 5 minutes, the furnace-treated samples continued to undergo subtle developments out to 10 minutes. Furthermore, the microwave sample XRD phases were narrow and highly crystalline at 5 minutes, while the width of the furnace-treated XRD phases continued to decrease in width out to 60 minutes. Again, the coating microstructures from both heat treatment techniques mirrored each other at each treatment time.
- The thermal spray coating microstructure exhibited a homogeneous response to microwave treatment. However, the physical mechanism accounting for the interaction of the electrical and magnetic components of the microwave with a discrete splat-based structure remains unclear. The lack of significant differentiation in response between the microwave and furnace treatment responses was attributed to the treatment temperature of 900 °C being too high above the critical phase transition temperatures, such that any beneficial effects of the microwave on the rate of phase development were overshadowed by the rapid thermally

driven phase developments in the furnace-treated samples. Future work at lower temperatures at and below the critical phase transitions and for significantly shorter times (<10 minutes) is recommended to highlight the potential benefits of microwave processing. Similarly, microwave trials without susceptors are recommended to gain a greater understanding of the microwave interaction with the thermal spray coating microstructure alone.

References

1. L.M. Berger, Hardmetals as Thermal Spray Coatings, *Powder Metall.*, 2007, **50**, p 205-214.
2. L.M. Berger, Application of Hardmetals as Thermal Spray Coatings, *Int. J. Refract Metal Hard Mater.*, 2015, **49**, p 350-364.
3. J. García, V. Collado Ciprés, A. Blomqvist, and B. Kaplan, Cemented Carbide Microstructures: A Review, *Int. J. Refract. Metals Hard Mater.*, 2019, **80**, p 40-68.

4. K. Jia and T.E. Fischer, Abrasion Resistance of Nanostructured and Conventional Cemented Carbides, *Wear*, 1996, **200**, p 206-214.

5. I. Konyashin, Approaching the 100th Anniversary of the Hardmetal Invention: From first WC-Co Samples Towards Modern Advanced Hardmetal Grades, *Int. J. Refract Metal Hard Mater.*, 2023, **111**, p 106113.

6. S. Norgren, J. García, A. Blomqvist, and L. Yin, Trends in the P/M Hard Metal Industry, *Int. J. Refract Metal Hard Mater.*, 2015, **48**, p 31-45.

7. R. Ahmed, N.H. Faisal, N.M. Al-Anazi, S. Al-Mutairi, F.L. Toma, L.M. Berger, A. Potthoff, E.K. Polychroniadis, M. Sall, D. Chaliampalias, and M.F.A. Goosen, Structure Property Relationship of Suspension Thermally Sprayed WC-Co Nanocomposite Coatings, *J. Therm. Spray Technol.*, 2014, **24**, p 357-377.

8. O. Ali, R. Ahmed, N.H. Faisal, N.M. Alanazi, L.M. Berger, A. Kaiser, F.L. Toma, E.K. Polychroniadis, M. Sall, Y.O. Elakwah, and M.F.A. Goosen, Influence of Post-Treatment on the Microstructural and Tribomechanical Properties of Suspension Thermally Sprayed WC–12 wt.%Co Nanocomposite Coatings, *Tribol. Lett.*, 2017, **65**, p 33.

9. H. Engqvist, H. Högberg, G.A. Botton, S. Ederyd, and N. Axén, Tribofilm Formation on Cemented Carbides in Dry Sliding Conformal Contact, *Wear*, 2000, **239**, p 219-228.

10. V. Rajinikanth and K. Venkateswarlu, An Investigation of Sliding Wear Behaviour of WCCo Coating, *Tribol. Int.*, 2011, **44**, p 1711-1719.

11. P.H. Shipway and J.J. Hogg, Dependence of Microscale Abrasion Mechanisms of WC-Co Hardmetals on Abrasive Type, *Wear*, 2005, **259**, p 44-51.

12. R.J.K. Wood, Tribology of Thermal Sprayed WC-Co Coatings, *Int. J. Refract Metal Hard Mater.*, 2010, **28**, p 82-94.

13. L.M. Berger, P. Sassatelli, J. Potschke and P. Puddu, Study of Binary WC- and Cr3C2-Based Hardmetal Compositions for Thermal Spray Coatings in: 19th Plansee Seminar, Plansee Group, Reutte, Austria, 2017, HM 82/81-14

14. S. Matthews, Development of High Carbide Dissolution/Low Carbon Loss Cr3C2-NiCr Coatings by Shrouded Plasma Spraying, *Surf. Coat. Technol.*, 2014, **258**, p 886-900.

15. S. Matthews, J. Ansbro, C.C. Berndt, and A.S.M. Ang, Carbide Dissolution in WC-17Co Thermal Spray Coatings: part 1-Project Concept and As-Sprayed Coatings, *J. Alloys Compd.*, 2021, **856**, p 157464.

16. S. Matthews and L.-M. Berger, Long-Term Compositional/Microstructural Development of Cr3C2-NiCr Coatings at 500 °C, 700 °C and 900 °C, *Int. J. Refract Metal Hard Mater.*, 2016, **59**, p 1-18.

17. S. Matthews, M. Bhagvandas, and L.M. Berger, Creation of Modified Cr3C2–NiCr Hardmetal Coating Microstructures Through Novel Processing, *J. Alloys Compd.*, 2020, **824**, p 153868.

18. S. Matthews, F. O'Neil, and P. Prasad, Phase Transformations in WC-Cr3C2-Ni Thermal Spray Coatings Under Low, Medium and high thermal Input: Part 1 – Feedstock and As-Sprayed Coating Characterisation, *Int. J. Refract Metal Hard Mater.*, 2022 https://doi.org/10.1016/j.ijrmhm.2022.106080

19. S. Zimmermann, H. Keller, and G. Schwier, *Improved coating properties by optimised carbide powders for modern HVOF systems, HVOF-Kolloquium*, Gemeinschaft Thermisches Spritzen EV, Erding, 2006, p 31-37

20. H.L. De Villiers Lovelock, Powder/Processing/Structure Relationships in WC-Co Thermal Spray Coatings: A Review of the Published Literature, *J. Therm. Spray Technol.*, 1998, **7**, p 357-373.

21. R. Schwetzke and H. Kreye, Microstructure and Properties of Tungsten Carbide Coatings Sprayed with Various High-Velocity Oxygen Fuel Spray Systems, *J. Therm. Spray Technol.*, 1999, **8**, p 433-439.

22. J.C. Han, M. Jafari, C.G. Park, and J.B. Seol, Microstructure-Property Relations in WC-Co Coatings Sprayed from Combinatorial Ni-Plated and Nanostructured Powders, *Mater Charact*, 2017, **129**, p 207-216.

23. C.J. Li and G.J. Yang, Relationships Between Feedstock Structure, Particle Parameter, Coating Deposition, Microstructure and Properties for Thermally Sprayed Conventional and Nanostructured WC-Co, *Int. J. Refract Metal Hard Mater.*, 2013, **39**, p 2-17.

24. S. Matthews, J. Ansbro, C.C. Berndt, and A.S.M. Ang, Thermally Induced Metallurgical Transformations in WC-17Co Thermal Spray Coatings as a Function of Carbide Dissolution: Part 2—Heat-Treated Coatings, *Int. J. Refract. Metals Hard Mater.*, 2021, **96**, p 105486.

25. Y.K. Cheong, J. Calvo-Castro, L. Ciric, M. Edirisinghe, E. Cloutman-Green, U.E. Illangakoon, Q. Kang, S. Mahalingam, R.K. Matharu, R.M. Wilson, and G. Ren, Characterisation of the Chemical Composition and Structural Features of Novel Antimicrobial Nanoparticles, *Nanomaterials*, 2017, **7**, p 152.

26. M. Gupta and W.W.L. Eugene, *Chapter 4 microwave heating and metal-based materials, microwaves and metals*, John Wiley and Sons, Hoboken, 2007, p 65-157

27. R.R. Mishra and A.K. Sharma, Microwave-Material Interaction Phenomena: Heating Mechanisms, Challenges and Opportunities in Material Processing, *Compos. A Appl. Sci. Manuf.*, 2016, **81**, p 78-97.

28. R. Roy, D. Agrawal, J. Cheng, and S. Gedevanlshvili, Full Sintering of Powdered-Metal Bodies in a Microwave Field, *Nature*, 1999, **399**, p 668-670.

29. K. Saitou, Microwave Sintering of Iron, Cobalt, Nickel, Copper and stainless steel powders, *Scripta Mater.*, 2006, **54**, p 875-879.

30. P. Muthusamy, M. Mohanraj, T. Ramkumar, and M. Selvakumar, Effect of Microwave Sintering on the Microstructure and Tribological Behavior of Ti-3Al-2.5 V-xWC Composite, *Tribol. Int.*, 2022, **174**, p 107714.

31. J. Sun, W. Wang, and Q. Yue, Review on Microwave-Matter Interaction Fundamentals and Efficient Microwave-Associated Heating Strategies, *Materials*, 2016, **9**, p 231.

32. D. Agrawal, J. Cheng, P. Seegopaul, and L. Gao, Grain Growth Control in Microwave Sintering of Ultrafine WC-Co Composite Powder Compacts, *Powder Metall.*, 2000, **43**, p 15-16.

33. R. Rumman, L.C. Chuan, J.S. Quinton, and R. Ghomashchi, Understanding the Potential of Microwave Sintering on WC—Co, *Int. J. Refract Metal Hard Mater.*, 2019, **81**, p 7-14.

34. B.R. Sunil, D. Sivaprahasam, and R. Subasri, Microwave Sintering of Nanocrystalline WC-12Co: Challenges and Perspectives, *Int. J. Refract Metal Hard Mater.*, 2010, **28**, p 180-186.

35. A. Amini, K.I. Ohno, T. Maeda, and K. Kunitomo, Effect of the Ratio of Magnetite Particle Size to Microwave Penetration Depth on Reduction Reaction Behaviour by H2, *Sci. Rep.*, 2018, **8**, p 15023.

36. J. Cheng, R. Roy, and D. Agrawal, Experimental Proof of Major Role of Magnetic Field Losses in Microwave Heating of Metal and Metallic Composites, *J. Mater. Sci. Lett.*, 2001, **20**, p 1561-1563.

37. K.I. Rybakov and V.E. Semenov, Microwave Heating of Electrically Conductive Materials, *Radiophys. Quantum Electron.*, 2005, **48**, p 888-895.

38. K.I. Rybakov, V.E. Semenov, S.V. Egorov, A.G. Eremeev, I.V. Plotnikov, and Y.V. Bykov, Microwave Heating of Conductive Powder Materials, *J. Appl. Phys.*, 2006, **99**, p 023506.

39. G. Veltl, F. Petzoldt, P.P. A, Effects of microwaves on sintering processes, in: Proceedings PM2004 World Congress, Vienna, 2004, Paper 83

40. R. Bao and J. Yi, Densification and Alloying of Microwave Sintering WC-8 wt.%Co Composites, *Int. J. Refract. Metals Hard Mater.*, 2014, **43**, p 269-275.

41. K. Rödiger, K. Dreyer, T. Gerdes, and M. Willert-Porada, Microwave Sintering of Hardmetals, *Int. J. Refract Metal Hard Mater.*, 1998, **16**, p 409-416.

42. S.A.A. Alem, R. Latifi, S. Angizi, F. Hassanaghaei, M. Aghaahmadi, E. Ghasali, and M. Rajabi, Microwave Sintering of Ceramic Reinforced Metal matrix composites and Their Properties: A Review, *Mater. Manuf. Processes*, 2020, **35**, p 303-327.

43. R. Bao and J. Yi, Effect of Sintering Atmosphere on Microwave Prepared WC–8wt.%Co Cemented Carbide, *Int. J. Refract. Metals Hard Mater.*, 2013, **41**, p 315-321.

44. E. Breval, J.P. Cheng, D.K. Agrawal, P. Gigl, M. Dennis, R. Roy, and A.J. Papworth, Comparison Between Microwave and Conventional Sintering of WC/Co Composites, *Mater. Sci. Eng. A*, 2005, **391**, p 285-295.

45. S.R. Medabalimi, M.R. Ananthu, S. Gudala, and M.R. Ramesh, Effect of Microwave Hybrid Heating on High-Temperature Adhesive Wear Behavior of High-Velocity Oxygen Fuel-Sprayed WC-CrC-Ni and WC-Co/NiCrFeSiB Coatings, *J. Mater. Eng. Perform.*, 2022, **32**(19), p 8612-8624.

46. S. Zafar and A.K. Sharma, Structure-Property Correlations in Nanostructured WC-12Co Microwave Clad, *Appl. Surf. Sci.*, 2016, **370**, p 92-101.

47. S. Bansal, D. Gupta, and V. Jain, Analysis of Susceptor Temperature During Microwave Heating and Characterization of Ni-30Cr3C2 clads, *Proc. Inst. Mech. Eng. Part L: J. Mater.: Design Appl.*, 2020, **234**, p 881-894.

48. S. Kaushal, D. Gupta, and H. Bhowmick, On Surface Modification of Austenitic Stainless Steel Using Microwave Processed Ni/Cr3C2 Composite Cladding, *Surf. Eng.*, 2018, **34**, p 809-817.

49. S. Kaushal, D. Singh, D. Gupta, and V. Jain, Processing of Ni–WC–Cr 3 C 2 -Based Metal Matrix Composite Cladding on SS-316L Substrate Through Microwave Irradiation, *J. Compos. Mater.*, 2019, **53**, p 1023-1032.

50. C.D. Prasad, S. Joladarashi, M.R. Ramesh, M.S. Srinath, and B.H. Channabasappa, Effect of Microwave Heating on Microstructure and Elevated Temperature Adhesive Wear Behavior of HVOF Deposited CoMoCrSi-Cr3C2 Coating, *Surf. Coat. Technol.*, 2019, **374**, p 291-304.

51. S. Matthews, Compositional Development as a Function of Spray Distance in Unshrouded/Shrouded Plasma-Sprayed Cr3C2-NiCr Coatings, *J. Therm. Spray Technol.*, 2015, **24**, p 515-533.

52. S. Matthews, A. Asadov, S. Ruddell, and L.M. Berger, Thermally Induced Metallurgical Processes in Cr_3C_2-NiCr Thermal Spray Coatings as a Function of Carbide Dissolution, *J. Alloy. Compd.*, 2017, **728**, p 445-463.

53. X. Ouyang, P. Cao, S. Huang, W. Zhang, Z. Huang, and W. Gao, Microwave-Assisted Synthesis of High Dielectric Constant CaCu3Ti4O12 from Sol-Gel Precursor, *J. Electron. Mater.*, 2015, **44**, p 2243-2249.

54. S. Matthews, B. James, and M. Hyland, The Role of Microstructure in the High Temperature Oxidation Mechanism of Cr3C2-NiCr Composite Coatings, *Corros. Sci.*, 2009, **51**, p 1172-1180.

55. C.J. Li, G.C. Ji, Y.Y. Wang, and K. Sonoya, Dominant Effect of Carbide Rebounding on the Carbon Loss During High Velocity Oxy-Fuel Spraying of Cr3C2-NiCr, *Thin Solid Films*, 2002, **419**, p 137-143.

56. T.Y. Velikanova, A.A. Bondar, and A.V. Grytsiv, Chromium-Nickel-Carbon (Cr-Ni-C) Phase Diagram, *J. Phase Equilib.*, 1999, **20**, p 125-147.

57. M. Venkatraman, and J.P. Neumann, The C-Cr (Carbon-Chromium) System, *Bull. Alloy Phase Diagr.*, 1990, **11**, p 152-159.

58. P. Nash, The Cr-Ni (Chromium-Nickel) System, *Bull. Alloy Phase Diagr.*, 1986, **7**, p 466-476.

59. C.B. Pollock and H.H. Stadelmaier, The eta Carbides in the Fe-W-C and Co-W-C Systems, *Metall. Trans.*, 1970, **1**, p 767-770.

60. A.F. Guillermet, Thermodynamic Properties of the Co-W-C System, *Metall. Trans. A*, 1989, **20**, p 935-956.

61. A.S. Kurlov and A.I. Gusev, Tungsten Carbides: Structure, Properties and Application in Hardmetals, *Springer Ser. Mater. Sci.*, 2013, **184**, p 34-36.

62. P. Franke and D. Neuschütz, Binary systems. Part 2: Elements and Binary Systems from B – C to Cr – Zr · Co-W: Datasheet from Landolt-Börnstein - Group IV physical chemistry · Volume 19B2: "Binary systems. Part 2: elements and binary systems from B – C to Cr – Zr" in SpringerMaterials, in: P. Franke, D. Neuschütz (Eds.), Springer, Berlin

63. H. Okamoto, Co-W (Cobalt-Tungsten), *J. Phase Equilib. Diffus.*, 2008, **29**, p 119-119.

64. V. Ramnath and N. Jayaraman, Quantitative Phase Analysis by X-ray Diffraction in the Co-W-C System, *J. Mater. Sci. Lett.*, 1987, **6**, p 1414-1418.

65. S. Matthews, M. Hyland, and B. James, Microhardness Variation in Relation to Carbide Development in Heat Treated Cr3C2-NiCr Thermal Spray Coatings, *Acta Mater.*, 2003, **51**, p 4267-4277.

66. Z.G. Ban and L.L. Shaw, Characterization of Thermal Sprayed Nanostructured WC-Co Coatings Derived from Nanocrystalline WC-18wt.%Co Powders, *J. Therm. Spray Technol.*, 2003, **12**, p 112-119.

67. X. Chen, C. Li, Q. Gao, X. Duan, and H. Liu, Comparison of Microstructure, Microhardness, Fracture Toughness, and Abrasive Wear of WC-17Co Coatings Formed in Various Spraying Ways, *Coatings*, 2022, **12**, p 814.

68. M. Gupta and W.W.L. Eugene, *Chapter 2 microwaves—theory, microwaves and metals*, JOHN WILEY AND SONS, HOBOKEN, 2007, p 25-41

69. H. Wang, T. Webb, and J.W. Bitler, Study of Thermal Expansion and Thermal Conductivity of Cemented WC-Co Composite, *Int. J. Refract Metal Hard Mater.*, 2015, **49**, p 170-177.

70. Y. Zhang and F. Li, Robust Half-Metallic Ferromagnetism in Cr3C2 MXene, *J. Magn. Magn. Mater.*, 2017, **433**, p 222-226.

71. M. Javid, X. Jiang, Y. Gao, L. Zhao, X. Zhang, A. Xu, A. Farid, M.F. Saleem, X. Zuo, Y. Zhao, L. Pan, and X. Dong, Experimental and Theoretical Validation of room Temperature Intrinsic Ferromagnetism in cr3c2 due to Interstitial Carbon Atoms, *Phys. Status Solidi - Rapid Res. Lett.*, 2022, **16**, p 2200192.

72. M. Javid, X. Qu, Y. Zhao, F. Huang, A. Farid, H. Zhang, A. Shah, K.A. Sammed, Y. Duan, Z. Zhang, L. Pan, and X. Dong, Synthesis of Hexagonal-Shaped Cr3C2@C Nanoplatelets and Role of Their Intrinsic Properties Towards Microwave absorption, *Mater. Lett.*, 2021, **288**, p 129329.

73. J. Yang, Z. Xiao, F. Yang, H. Chen, X. Wang, and S. Zhou, Microstructure and Magnetic Properties of NiCrMoAl/WC Coatings by Laser Cladding: Effect of WC Metallurgical Behaviors, *Surf. Coat. Technol.*, 2018, **350**, p 110-118.

74. F. Otsubo, H. Era, K. Kishitake, and T. Uchida, Properties of Cr3C2-NiCr Cermet Coating Sprayed by High Power Plasma and High Velocity Oxy-Fuel Processes, *J. Therm. Spray Technol.*, 2000, **9**, p 499-504.

75. M. Suarez, S. Bellayer, M. Traisnel, W. Gonzalez, D. Chicot, J. Lesage, E.S. Puchi-Cabrera, and M.H. Staia, Corrosion Behavior of Cr3C2–NiCr Vacuum Plasma Sprayed Coatings, *Surf. Coat. Technol.*, 2008, **202**, p 4566-4571.

76. P.H. Suegama, N. Espallargas, J.M. Guilemany, J. Fernández, and A.V. Benedetti, Electrochemical and Structural Characterization of Heat-Treated Cr3C2 – NiCr Coatings, *J. Electrochem. Soc.*, 2006, **153**, p B434.

77. J.F. Shackelford, Y.-H. Han, S. Kim, and S.-H. Kwon, *CRC materials science and engineering handbook*, CRC Press, Boca Raton, 2015.

78. D.L. Houck and R.F. Cheney, Comparison of Properties of Cr_3C_2-Ni-Cr Coatings Thermally Sprayed from Pre-Alloyed and Mechanically Mixed Powders, *Thin Solid Films*, 1984, **118**, p 507-513.

79. Z. Marcano, J. Lesage, D. Chicot, G. Mesmacque, E.S. Puchi-Cabrera, and M.H. Staia, Microstructure and Adhesion of Cr_3C_2-NiCr Vacuum Plasma Sprayed Coatings, *Surf. Coat. Technol.*, 2008, **202**, p 4406-4410.

80. J.D. Reardon, R. Mignogna, and F.N. Longo, Plasma- and Vacuum-Plasma-Sprayed Cr_3C_2 Composite Coatings, *Thin Solid Films*, 1981, **83**, p 345-351.

81. J.F. Pelton, J.M. Koffskey(Jr), Patent—Coating composition, method of application, and product thereof (Union Carbide Corp), US 3,150,938, filed: 9 June 1960, granted 29 September 1964 (also GB 929,205), in, 1964, pp 1-3.

82. J.A. Sue and R.C. Tucker Jr., High Temperature Erosion Behavior Tungsten- and Chromium-Carbide-Based Coatings, *Surf. Coat. Technol.*, 1987, **32**, p 237-248.

83. K. Ikeda, ELectrical Resistivity of Nickel Cobalt and Their Alloys, *Trans. Japan Inst. Metals*, 1988, **29**, p 183-190.

84. T. Farrell and D. Greig, The Electrical Resistivity of Nickel and Its Alloys, *J. Phys. C Solid State Phys.*, 1968, **1**, p 1359-1369.

85. K. Korpiola, High temperature oxidation of metal, alloy and cermet powders in HVOF spraying process (PhD Thesis), Helsinki University of Technology, 2004.

86. V. Shukla, The Tunable Electric and Magnetic Properties of 2D MXenes and Their Potential Applications, *Mater. Adv.*, 2020, **1**, p 3104-3121.

87. J.C. Slater, The Ferromagnetism of Nickel, *Phys. Rev.*, 1936, **49**, p 537-545.

88. J. Li and C. Ding, Improvement in the Properties of Plasma-Sprayed chromium carbide coatings using nickel-clad powders, *Surf. Coat. Technol.*, 2000, **130**, p 15-19.

89. B. Legendre and M. Sghaier, Curie Temperature of Nickel, *J. Therm. Anal. Calorim.*, 2011, **105**, p 141-143.

90. V.A. Serban, I. Malaescu, A. Ercuta, C.N. Marin, N. Stefu, C. Opris, C. Codrean, D. Utu, Magnetic properties of the WC-Co cermet powders, in: AIP Conference Proceedings, 2010, pp 113-117

91. H. Keller, E. Pross, and G. Schwier, *Influence of the powder type on the structure and the properties of chromium carbide/nickel chromium coatings, in*, Starck Publication, H.C, 2000.